

Universidade de Coimbra
Faculdade de Ciências e Tecnologia
Departamento de Física

High dielectric constant oxides for CMOS technology

Marco Alberto

Projecto em Engenharia Física
Ramo de Metrologia e Qualidade, Julho 2017

Abstract

Hydrogen in the paramagnetic rare earth oxide Nd_2O_3 (neodymium sesquioxide) was investigated through muon spin spectroscopy measurements obtained at the EMU instrument of the ISIS Facility (Rutherford Appleton Laboratory, United Kingdom). Muonium, as a light pseudo-isotope of hydrogen, was used to mimic the electronic configurations of hydrogen. Both the donor-like configuration at an oxygen-bound site and the acceptor-like configuration at an interstitial site have been identified. A fast relaxing component is also observed, which is identified with a transition muonium state occurring during the formation. This fast component presents a negative frequency shift that we interpret as an effect of the paramagnetic magnetization at low-temperatures, in conjunction with ancillary magnetometry measurements performed at the TAIL Facility of the University of Coimbra. The temperature dependence of the fractions allows identifying the conversion barrier from the interstitial configuration to the oxygen-bound configuration with an activation energy of 0.5 eV, as well as the barrier height from the transition state to the oxygen-bound configuration at 0.15 eV. The diffusion of the positively charged species above room temperature is also identified as an activated process with an activation energy of 0.14 eV. This is the first attempt to characterize the hydrogen configurations at a paramagnetic oxide using the sensitive muon probe, and the results clearly show the feasibility of the method.

Contents

Abstract	i
1 Hydrogen in oxides	1
1.1 Hydrogen in oxides: overview	1
1.2 Applications	3
1.3 μ SR in Paramagnetic Oxides. A Brave New World	4
2 Experimental Details	5
2.1 Muon spin spectroscopy (μ SR)	5
2.1.1 Production of polarized muon beam	6
2.1.2 Muon decay and the μ SR signal	7
2.1.3 Muon facilities and spectrometers	11
2.2 Magnetometry	13
3 Basic magnetic characterization of the sample	19
3.1 Temperature and field dependent measurements	19
3.2 Temperature dependence of susceptibility: Curie-Weiss model	21

3.3	Determination of magnetic moment of Nd^{3+} from high temperature susceptibility	23
3.3.1	Temperature dependence of the susceptibility at low temperature	24
3.4	A metrology digression: rare-earth oxides as calibration standards in magnetometry	28
4	Muon Spin Spectroscopy Results	33
4.1	Fast to slow conversion below $T= 300$ K	37
4.1.1	Frequency shift of the fast component	38
4.2	Recovery of the missing fraction above 300 K	39
4.2.1	Motional narrowing of the slow component	40
4.3	Discussion	41
4.3.1	Slow component	41
4.3.2	Missing fraction	42
4.3.3	Fast component	43
5	Conclusion and Future Perspectives	47
5.1	Conclusions	47
5.2	Future Perspectives	48
5.2.1	Repolarization at low temperatures	48
5.2.2	Frequency shift	48
5.2.3	Extension to other rare-earth oxides	49
	Bibliography	52

List of Tables

3.1	Linear and quadratic Zeeman effect parameters a_j and b_j estimated from the fit in Fig. 3.7	27
3.2	Values of the susceptibility of Pd at different temperatures	29
3.3	Rare-earth oxides investigated.	30
3.4	Values of S,L,J, g_J , p_{eff} for each rare-earth ions	31

List of Figures

1.1	Scheme of a MOSFET (taken from [Mos]). A current may exist between the n-type source and drain through the p-type channel when a tension is applied to the gate, leading to an inversion configuration.	3
2.1	The decay of the positive pion.	6
2.2	Angular distribution of positron decay with relation to the muon spin direction (at 0 degree). We represent the cases of maximum positron energy, as well as the result of integration over all energies (red line).	7
2.3	The basic setup of the muon experiment	8
2.4	Counts of the silver sample for each detector. The red dots are the counts of the forward detectors and the dots in green are the counts of the backward detectors	10
2.5	Experimental asymmetry as a function of time without introducing the geometrical correction ($\alpha=1$). The oscillations are clearly shifted towards negative asymmetries due to the predominance of the B detector.	10
2.6	Experimental asymmetry as a function of time including the geometrical correction ($\alpha=0.94$). The asymmetry now is centered at $A=0$	11
2.7	Model of the ISIS facility: protons are accelerated in a synchrotron(appear left corner) and redirected to a carbon target before reaching the spallation source. Positive muons(green) are produced and redirected to the muon spectrometers .	12

2.8	Image of the EMU spectrometer, where the positron detectors are clearly visible.	13
2.9	A general scheme of the functional principle of the VSM. 1)sample, 2) sample holder, 3) pickup coils. The horizontal lines represent the magnetic field and the vertical line represents the vibration of the sample.	14
2.10	PPMS magnetometer of the TAIL facility of the University of Coimbra	14
2.11	Moment magnetic of Pd sample as a function of applied magnetic field, for T=298 K	16
2.12	The Dynacool Cryostat showing the components of the Cryostat Control System, Chamber Temperature Control System and Magnetic Control System.	18
3.1	Magnetic moment of the Nd ₂ O ₃ sample as a function of temperature, with an applied field of 100 Oe.	20
3.2	Magnetic moment of the Nd ₂ O ₃ sample as a function of applied magnetic field, for T=1.8 K (a) and T=50 K (b)	20
3.3	Inverse magnetic susceptibility of Nd ₂ O ₃ as a function of temperature.	21
3.4	The ground state of Nd ³⁺	23
3.5	Magnetometry of Nd ₂ O ₃ , plotting the inverse susceptibility against the temperature. The blue line is a fit of the Curie-Weiss law in the range of temperatures between 200 K and 300 K	24
3.6	Energy levels of Nd ³⁺ according to [HMG67]	25
3.7	Fit to the magnetic susceptibility of Nd ₂ O ₃ including the crystal-field effects, as described in the text.	27
3.8	Inverse magnetic susceptibility of Gd ₂ O ₃ as a function of temperature.	30
3.9	Inverse magnetic susceptibility of Dy ₂ O ₃ as a function of temperature.	30

3.10	Comparison of the expected and experimental value of the effective number of Bohr magnetons for several rare-earth ions, p_{eff} . The error bars are smaller than the circles.	31
4.1	Time spectrum for a polycrystalline Nd_2O_3 sample at $T=50$ K and a transverse applied magnetic field $B=0.01$ T. (a) full data: the line represents the fitted slowly relaxing component, as detailed in the text. (b) fast relaxing component only, obtained from the fit as detailed in the text.	33
4.2	Temperature dependence of the slowly relaxing and of the fast relaxing components (white circles and black circles, respectively).	35
4.3	Temperature dependence of the relaxation of the fast component.	36
4.4	Temperature dependence of the precession frequency of the fast component, for an applied transverse magnetic field $B=0.01$ T. The dashed line is the value of precession frequency of a silver calibration sample in the same geometry.	36
4.5	Temperature dependence of the slowly relaxing and of the fast relaxing components (white circles and black circles, respectively). The lines represent a common fit to the conversion from the fast to the slow component, as detailed in the text, with $E_a=0.15(3)$ eV	38
4.6	Temperature dependence of the relaxation of the fast component. The line is a fit of a conversion model from the fast component to the slow component, as explained in the text, with $E_a=0.15(3)$ eV.	38
4.7	Temperature dependence of the slowly relaxing component. The full line is a fit to the conversion of the missing fraction to the slow component, as explained in the text, with $E_a=0.5(1)$ eV.	40
4.8	Temperature dependence of the relaxation of the slow component, above room temperature. The line is a fit of an activated process, as explained in the text below.	40

4.9	Crystal structure of Nd_2O_3 . The red circles are the oxygen ions and white circles are Nd ions.	42
4.10	Final step in muon implantation: Neutral (Mu^0) and charged (Mu^+) muons come to rest at an interstitial site in the unrelaxed lattice (marked by *). Mu^+ forms directly the final bound configuration, but Mu^{0*} may go through an intermediate (transition) state before the final configuration is formed.	44
4.11	Schematic representation of the total energy for the conversion from atom-like interstitial to oxygen-bound muonium in Nd_2O_3 , including the value of the height of the energy barriers determined experimentally.	46
5.1	Time spectrum for a polycrystalline Sm_2O_3 sample at $T=50$ K and a transversal applied magnetic field $B=0.01\text{T}$. The upper graphic is the representation of the fast component and in the bottom plot we present the full data; the red line is the fit to the slow component only.	49

Chapter 1

Hydrogen in oxides

1.1 Hydrogen in oxides: overview

The production process of semiconductors is likely to introduce unintended hydrogen atoms in significant concentrations. A particularly relevant example is that of the deposition of thin-film high-k dielectric oxides by atomic-layer deposition, a technique which is known to provide films with enhanced quality [RN09]. The concentration of hydrogen atoms in ALD grown films has been measured to be of the order of 1%, an extraordinarily large number [PPN05]. Although hydrogen is the simplest of atoms, it has the particularity of showing complex behaviour as a impurity in many materials, deeply affecting their electrical and optical properties [VdWN03] [Nic99].

One of the most significant effects of the hydrogen impurity is the passivation/activation of other defects and impurities. This phenomenon consists in the formation of a complex between two impurities/defects, changing in that way the electrical and optical properties of both, with respect to the situation where they are not bounded [VGW⁺08].

A relevant example is amorphous Si, where hydrogen removes the unwanted electrically active defect levels, associated to the existing dangling bonds [LCC08]. Another example is GaN, where the hydrogen form complexes with Mg or Zn, passivating those impurities. The under-

standing of the effect of the hydrogen in GaN was a critical step in the development of blue LEDs [BRI14]. Hydrogen can also act as an activating impurity, such as in Ge where the hydrogen atoms are trapped in otherwise electrically inactive interstitial impurities of C and Si, thus forming electrically active complexes [HJF80] [DNZ⁺04].

Hydrogen can also be isolated within semiconductors and the understanding of the isolated hydrogen impurity is not only a relevant aspect per se, but it also constitutes a crucial step in order to address more complex behaviours. Hydrogen is known to act mostly as a compensating impurity. As an amphoteric impurity, it will act as a donor in p-type material and as an acceptor in n-type materials, always counteracting the prevailing conductivity [VdW06]. This effect occurs in Si, Ge and in other semiconductors such as GaAs [LCG⁺06] and GaN [NVdW95].

Another important behaviour of the isolated hydrogen impurity is acting as a dopant. Hydrogen can then act as a source of conductivity. Hydrogen in some materials can change the conductivity behaviour, like in ZnO [GAV⁺01]. This effect occurs in some semiconductors like CdS, CdSe and ZnO [GAV⁺01] [VdW00].

In order to address the behaviour of hydrogen in semiconductors and insulators, the complementarity between theory and experiment proves to be essential. Among the theoretical contributions a theoretical model proposed by Van de Walle and Neugebauer, allow to establish a connection between the electrical characteristics and the line-up of band structures of the host materials on an absolute energy scale. This approach is based on density-functional theory (DFT) within the local density approximation (LDA) and the pseudopotential-plane-wave method.

The model of Van de Walle and Neugebauer predicts the behaviour of hydrogen in a number of semiconductors, including GaN (amphoteric behaviour) and in ZnO (shallow donor) [VdW06] [VdWN03].

Experimentally, the microscopic characterization of isolated hydrogen has been done directly in very few cases by electron paramagnetic resonance (EPR/ electron-nuclear double resonance (ENDOR)). However, this technique requires high concentrations of hydrogen. Most of the

experimental microscopic information about isolated hydrogen has been obtained by the muon spin spectroscopy technique based on the implantation of positive muons. This information about hydrogen obtained with this technique relies on the formation of muonium (the bound state of a positive muon and of an electron) which mimics the electronic properties of hydrogen since muonium is a light pseudo-isotope. This technique has allowed to obtain the microscopic characterization of the hydrogen states in many materials (such as GeAs or Cd [VGW⁺08], [VGW⁺07]). In the very few cases where both μ SR and EPR-ENDOR DATA are available, the techniques provide similar results [VVA⁺15][HHL⁺02].

1.2 Applications

CMOS (Complementary Metal Oxide Semiconductor) technology has a great spectrum of applications, like in microprocessors, memories and the technology of MOSFET (metal-oxide-semiconductor field-Effect Transistor) [SM08].

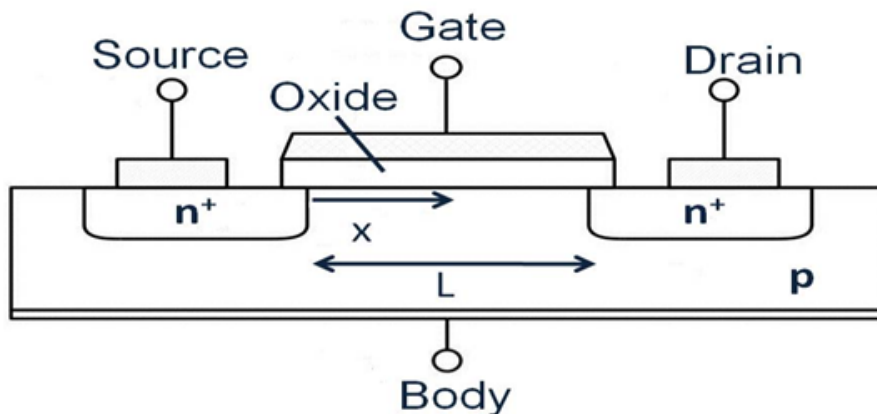


Figure 1.1: Scheme of a MOSFET (taken from [Mos]). A current may exist between the n-type source and drain through the p-type channel when a tension is applied to the gate, leading to an inversion configuration.

Figure 1.1 shows the basic structure of a p-MOSFET. The gate consists of a metallic contact on top of an insulating oxide. One of the current problems of CMOS technology is the thinning of the insulator layer. Traditionally, the insulator material used in CMOS technology was SiO_2 , but as the oxide width decreases it can no longer support the applied tension without electric

rupture [LFR⁺05][Rob04].

To address this problem, it is necessary to investigate materials with high dielectric constant (high-k). However, the interface between the high-k gate material and the metal gate may introduce significant variation in the device such as mobility degradation [Sah10]. Currently, HfO₂ is used to substitute SiO₂. HfO₂ is a high-k material but presents some problems, like the existence of random grain orientation, originating variations of the dielectric constant [Sah10].

Rare-earth oxides are placed as candidates to the next generation of insulators in CMOS technology. They present high relative permittivity and chemical stability [PPN05], [KPPN05], [NPP⁺05]. The introduction of rare-earth oxides CMOS technology implies the production of thin films: electron-beam evaporation or atomic deposition techniques have been developed [PPSN04]. However even the techniques producing films with the highest quality introduce significant quantities of hydrogen [FS07].

1.3 μ SR in Paramagnetic Oxides. A Brave New World

μ SR was been used very successfully to characterize the hydrogen configurations in semiconductors and insulators, but always in diamagnetic materials. The application of μ SR to paramagnetic rare-earth oxides in order to characterize the hydrogen configuration presents particular challenges: the muon spin is extremely sensitive to local magnetic fields. The effect of the local fields created by the paramagnetic rare-earth ions may affect the μ SR signal and bring additional difficulties to the interpretation, possibly preventing the extraction of useful information about the muonium configurations.

The main objective of this project was therefore to perform the first μ SR study on a paramagnetic rare-earth oxide. Some preliminary μ SR measurements had been performed by the Coimbra μ SR team and the most complete set of data is that of Nd₂O₃, where we have henceforth concentrated our efforts.

Chapter 2

Experimental Details

2.1 Muon spin spectroscopy (μ SR)

The theoretical basis of the muon spin spectroscopy (μ SR) technique has been laid out by Lee and Yang [LY56] and experimentally demonstrated by Garwin, Lederman and Weinrich [GLW57]. In 1957 Garwin and collaborators refers that "it seems possible that polarized positive and negative muons will become a powerful tool for exploring magnetic fields in nuclei, atoms and interatomic regions." [YDdR11].

Actually, positive muon spin spectroscopy is used in two main field of condensed matter physics. Firstly, in the determination of magnetic behaviour and of superconductivity behaviour, because the muon is a sensitive magnetometer. This means that, when the muon is inside the material, it will probe the local field and its time dependent signal will provide information about the local fields. It can be used to study magnetic and superconducting materials [SBK00], [Blu99].

Another application of this technique is the use of the muon as a light pseudo-isotope of hydrogen. The muonium atom is formed by an electron bound to a positive muon that can be thought in condensed matter physics and chemistry as a light pseudo isotope of hydrogen, due to the similarity of its electronic properties [VVA⁺14], [CDC⁺01].

2.1.1 Production of polarized muon beam

Because the muon is not stable (its lifetime is $2.2 \mu\text{s}$) it is necessary to create an indirect process to produce this particle. This process is composed by two phases. First, we must accelerate protons. The high energy protons will collide directly with a target made of a light element (e.g. carbon)[Beab]. Such collisions produce pions, as in the following process:



The positive pion is unstable and decays via the weak interaction:



The particle decays into a muon and a muonic neutrino (equation 2.2). The neutrino is a zero mass particle. Because of that, it has negative helicity. This means that the linear momentum is always anti-parallel to its spin. The pion has a spin equal to zero.

During the decay of the pion, conservation of linear momentum and angular momentum occur. The consequence of these two principles is that, when the pion is at rest in the target, the muon brings out a spin anti-parallel to its linear momentum, as shown in figure 2.1.



Figure 2.1: The decay of the positive pion.

2.1.2 Muon decay and the μ SR signal

The muon decays via weak interaction with a half-life of $2.2 \mu\text{s}$:



ν_e is the electron neutrino and $\bar{\nu}_\mu$ is the muonic anti-neutrino. The positrons are emitted with an energy ranging from 0 MeV up to 52.3 MeV. As a result of the weak interaction the decay does not follow the conservation of parity. The resulting positron is therefore preferentially emitted in the direction of the muon spin. The angular dependence of the probability of emission of the positron, as a function of the energy of the positron [LCK99], is represented in the figure 2.2

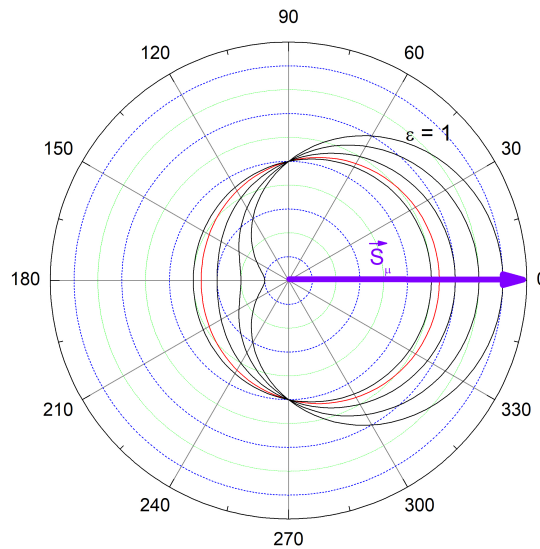


Figure 2.2: Angular distribution of positron decay with relation to the muon spin direction (at 0 degree). We represent the cases of maximum positron energy, as well as the result of integration over all energies (red line).

The probability of a positron being emitted in the direction of the muon spin is therefore much different from the probability of it being emitted opposite to the muon spin. A pair of detectors placed in these two directions therefore allows to monitor the time evolution of the muon spin polarization.

The basic setup is shown in figure 2.3

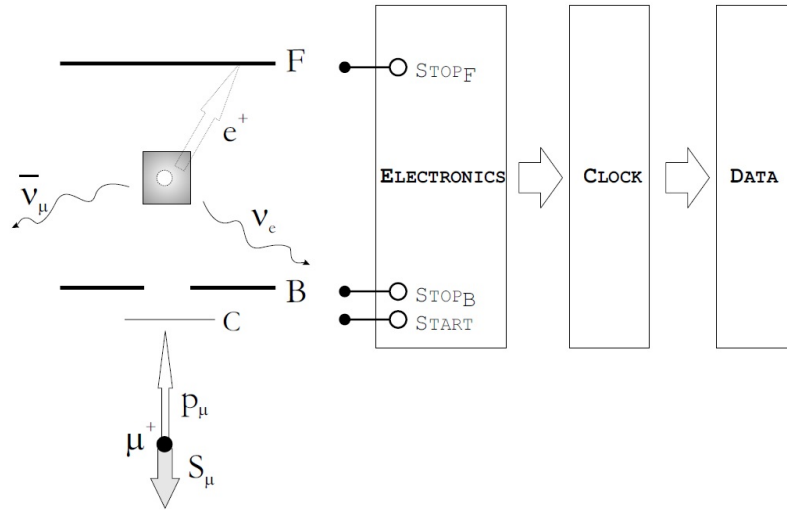


Figure 2.3: The basic setup of the muon experiment

The spin-polarized 4 MeV muon beam is implanted into the material. The muon beam is guided to the spectrometer with a series of dipole and quadrupole magnets from the muon target. In the simplest geometry, two detectors, are placed around the sample space, one in the front of the sample (F) and another in the back (B). The incoming muon comes across a scintillator and starts a chronometer, which is stopped with the detection of the emitted positron either on detector F or detector B.

The counts on each detector are different (Fig. 2.4). The number of counts in each detector can be described by the following equation:

$$N_D = B_D + N_0 \varepsilon_D [1 \pm A P_z(t)] \quad (2.4)$$

where:

- B_D is the background of each detector;
- N_0 multiplied by the number of detectors corresponds to the number of real events at time zero;
- ε_D is the efficiency of each detector;
- A is the intrinsic asymmetry of the detector arrangement. The counts are proportional

to $(1+A)$ in the case of fully polarized muons in the case of detector B, and for the case of detector F the counts are proportional to $(1-A)$;

- $P(z)$ is the time evolution of the z component of the polarization, where z is defined by the incoming beam direction;

We are interested in the time evolution of the muon spin polarization, that is reflected in the quantity A. Ideally, the experimental asymmetry in the emission of positron is nothing but the normalized difference $A_{exp} = \frac{N_F - N_B}{N_F + N_B}$. However, factors such as the intrinsic efficiencies of the detectors, the thickness of the sample or simply the geometrical off-centering of the sample with respect to the detectors affect the correct estimation of the asymmetry. A simple way to correct this is simply by giving additional weight to one of the detectors: $A_{exp} = \frac{N_F - \alpha N_B}{N_F + \alpha N_B}$. The correction parameter α can be determined, for each experimental geometry, by a calibration measurement at low transverse fields (typically 20 - 100G). The experimental asymmetry is here expected to oscillate at the Larmor frequency $\omega = B\gamma$ ($\gamma = 135.53\text{MHz/s}$). Without the correction α (i.e $\alpha=1$) the oscillations are not in the term of $A=0$, The correct α is defined so that A_{exp} oscillates in turn of $A_{exp}=0$ [LCK99] (Figs 2.5 and 2.6).

To determine the maximum instrumental asymmetry A at EMU, it is usually used a silver sample in weak-transversal fields. In this situation, the muon is subject only to the Zeeman interaction with the applied field. The precession of the spin of the muon with the applied field can be described by the Larmor frequency.

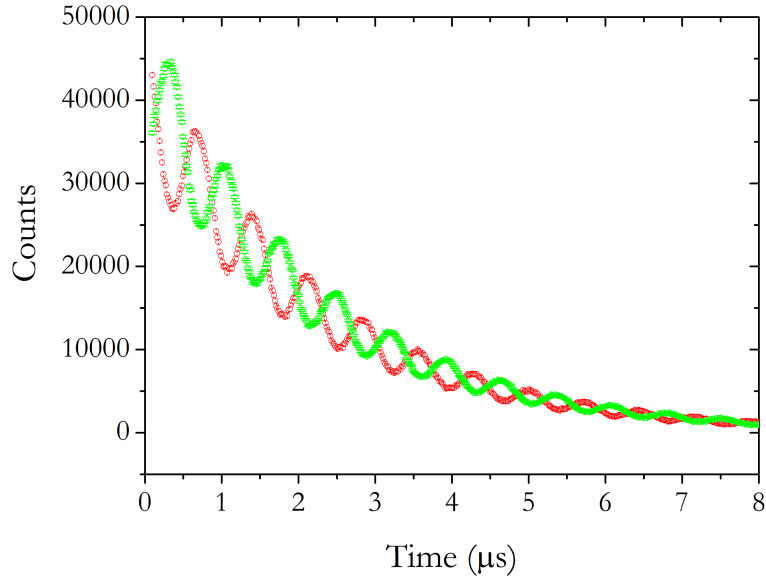


Figure 2.4: Counts of the silver sample for each detector. The red dots are the counts of the forward detectors and the dots in green are the counts of the backward detectors

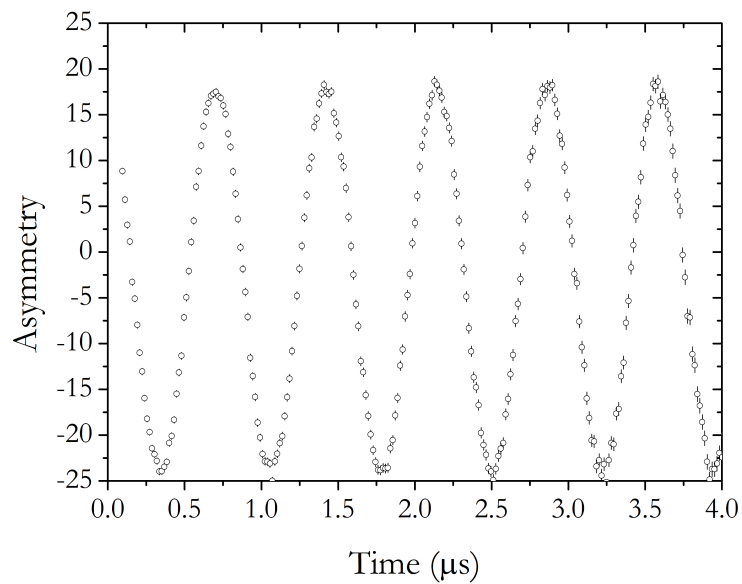


Figure 2.5: Experimental asymmetry as a function of time without introducing the geometrical correction ($\alpha=1$). The oscillations are clearly shifted towards negative asymmetries due to the predominance of the B detector.

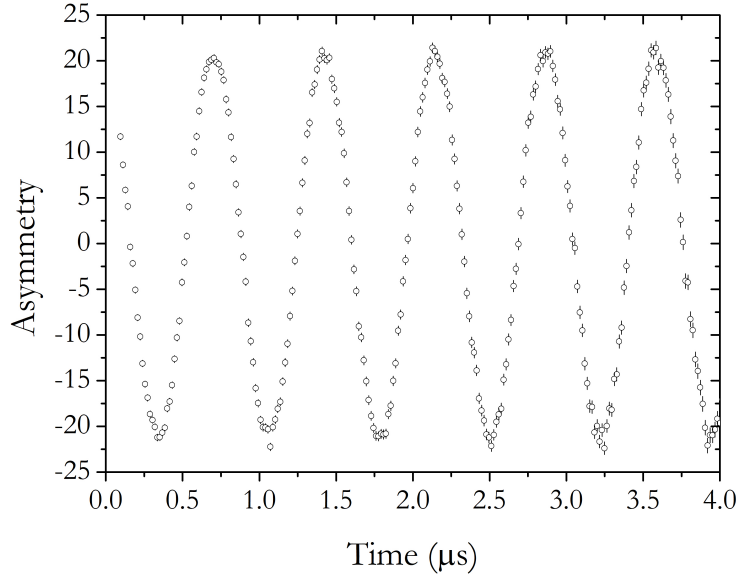


Figure 2.6: Experimental asymmetry as a function of time including the geometrical correction ($\alpha=0.94$). The asymmetry now is centered at $A=0$.

2.1.3 Muon facilities and spectrometers

The production of muons requires a source able to accelerate protons up to hundreds of MeV. For this, large-scale installations are required. Currently, four muon user facilities are available: the ISIS pulsed muon facility at the Rutherford Appleton Laboratory, in the United Kingdom[GCK⁺14], the Laboratory for muon spin spectroscopy at the Paul Scherrer Institut, in Switzerland[PSI]; the Centre for molecular and materials science at the Tri-university Meson Facility, TRIUMF[TRI], in Canada; and the J-Park facility, in Tokai, Japan [MSK⁺12].

The experimental data presented in this work were obtained at the ISIS facility in the United Kingdom. This is a pulsed source producing a 800 MeV proton beam. The produced spin-polarized beam of positive muons is directed to three muon spectrometers: EMU, MUSR and HiFi[Beaa] (Fig 2.7).



Figure 2.7: Model of the ISIS facility: protons are accelerated in a synchrotron(appear left corner) and redirected to a carbon target before reaching the spallation source. Positive muons(green) are produced and redirected to the muon spectrometers

In this work, the EMU spectrometer was used (Fig 2.8). It has 96 positron detectors. It has three axial rings forward and another three axial rings backward, each one with 16 detectors. The signal of the detectors is transferred by light guides to nearby photomultipliers, so that the local magnetic field does not affect the electronics. The signal acquired is treated with techniques of coincidence and anti-coincidence of signals, to make sure that the signal obtained in the detector is a true signal of the decay of the muon. The EMU spectrometer is optimized to work in longitudinal fields and zero field, but it can also work in tranverse field. The range of temperatures it operates are between 50 mK and 1500 K.

To produce the required magnetic fields, the appropriate electrical equipments are necessary. To produce longitudinal field the EMU is equipped with Helmholtz coils that can reach up to 4500G. To provide the transverse field, the EMU is equipped with two saddle coils that achieve up to 150G. To have zero field its necessary an electronic device that counters the earth magnetic field.To do it, the EMU has installed three pairs of coils to cancel the Earth magnetic field[INMS15].



Figure 2.8: Image of the EMU spectrometer, where the positron detectors are clearly visible.

2.2 Magnetometry

In chapter 1 we have seen that the characterization of the hydrogen configuration in Nd_2O_3 using the positive muon as a light pseudo-isotope of hydrogen presents particular challenges in the rare-earth paramagnetic oxides, since the muon is a very sensitive magnetic probe. In the course of this investigation, a detailed macroscopic characterization of the magnetic properties of Nd_2O_3 sample is envisaged. Macroscopic magnetometry measurements at the TAIL facility of the University of Coimbra were therefore undertaken.

The magnetometer used in this project is the PPMs DynaCool vibrating sample magnetometer (VSM) developed by Quantum Design. The basic working principle of vibrating sample magnetometry is the Faradays Law.

Fig 2.9 shows the functional principle of the VSM. The sample is introduced between the magnet, that applies an horizontal magnetic field. After the sample is introduced, it is set in vibration motion in the vertical direction. The oscillation motion of the sample promotes a voltage in the pickup coils. The induced voltage is proportional to the magnetization of the sample[BPJ03].

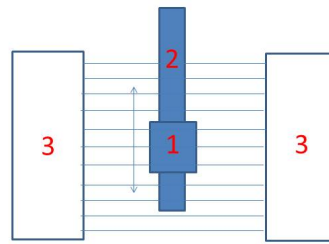


Figure 2.9: A general scheme of the functional principle of the VSM. 1) sample, 2) sample holder, 3) pickup coils. The horizontal lines represent the magnetic field and the vertical line represents the vibration of the sample.

The magnetometer installed at the TAIL facility of the University of Coimbra is shown in figure 2.10, when the following main components are identified[Dyn11]:

- Cryostat Assembly
- Pump Cabinet and Computer
- Cryocooler Compressor Assembly
- Helium Gas Bottle and Regulator



Figure 2.10: PPMS magnetometer of the TAIL facility of the University of Coimbra

The cryostat assembly includes the superconducting magnet and the sample chamber, which can be raised with a vertical movement. Two LED displays can be seen in front of the chamber,

which give information about the temperature and the magnetic field inside. We note that in particular cases the temperature of the chamber can be different from that of the sample, particularly if the process of cooling/ heating is fast and the sample is not in thermal equilibrium with the environment.

The Cryocooler compress assembly includes a circulation loop and a sealed scroll that is used for circulating helium past the sample chamber so that it cools the sample; a chamber/case pump, a low capacity scroll pump for evacuating the sample chamber during chamber pumping and purge operations and a Cryostat Controller Electronics, containing thermometers and heater circuits for managing the cryostat and gas-handling manifold, that contains solenoids valves, pressure gauges, pressure regulators, and various gas interconnections to manage the flow of gas.

All the hardware is controlled by the software (MultiVi) through a CAN network controller [Can]. The magnetic system in the sample space is created by two superconductivity solenoids. The field can achieve 9 T. The functioning of the superconducting magnet requires the superconductivity solenoids to be at low temperature (around a few Kelvin). As will be presented below, a complex cooling system is used to cool both the sample and the magnet.

The magnets are protected with a magnetic shield. The function of the shield is to enclose the magnetic field within the magnets.

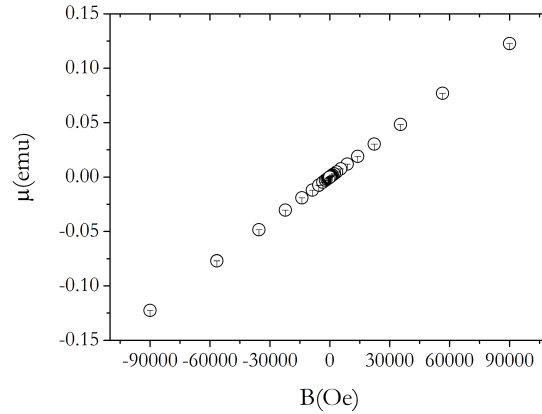


Figure 2.11: Moment magnetic of Pd sample as a function of applied magnetic field, for $T=298$ K

We note that the magnetic moment of the sample is directly measured by the magnetometer. The quantity is of course dependent on the size of the sample. In order to extract the relevant magnetic properties of the material (magnetization, magnetic susceptibility) it is therefore crucial to determine accurately the mass of the sample. An example is shown in the fig 2.11 for a palladium calibration sample.

Temperature control

As mentioned above, a complex cooling system (cryostat control engine) is used to cool both the engine space and the superconductivity solenoids. This is shown in figure 2.12.

Adiabatic expansion of helium is used as the cooling principle. If there is no exchange of energy between the system and the outside, the expansion of helium in a fixed volume leads to a decrease in pressure and to a corresponding decrease in temperature [Rad09].

In the first stage of the cooler, the system reaches 45 K. This stage is used to cool the support from room temperature, the first stage of cryopump and the electrical wiring. In this phase, the cooling proceeds by conduction through a small gas gap to the first stage of the cryocooler and other devices are cooled by direct contact.

In the second state of cooler, the system reaches 4 K and other components requiring this low temperature are cooled: the 4K plate, the superconducting magnet or the second stage of the

cryopump.

Two heaters in the system are used for warming: one for heating the main radiation shield to increase the temperature of the system and controlling the pretended temperature, the second to warm the 4 K plate.

Magneto-resistive Cernox thermometers are used [Tp]: these have the advantage that the electronic signal is proportional to the resistance and can be used in applications that work with slow temperatures [HL98]. One thermometer controls the main radiation field, which is in direct contact with in the first step cooler. A second thermometer is used to monitor the temperature of the 4 K plate. A third thermometer is used to control the temperature of the magnets.

Two pair of thermometers are placed at the sample space: one is localized above the isothermal region, and the other pair is localized approximately in the vertical center of the sample. The objective of having two pairs of thermometers is to provide information in order to reduce the thermal gradient in the sample chamber.

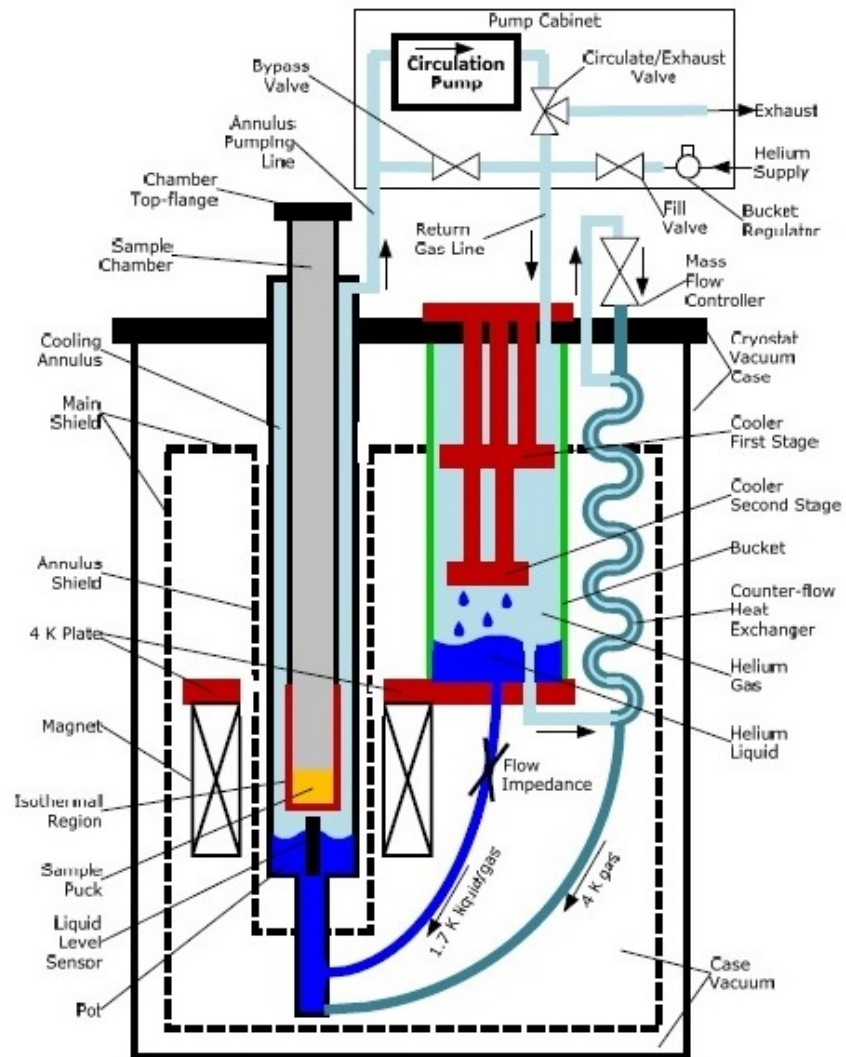


Figure 2.12: The Dynacool Cryostat showing the components of the Cryostat Control System, Chamber Temperature Control System and Magnetic Control System.

Chapter 3

Basic magnetic characterization of the sample

The use of muon spin spectroscopy to assess the hydrogen configurations in rare-earth oxides in general, and in Nd_2O_3 in particular, may be a difficult task due to the paramagnetic character of these materials. The being muon an extremely sensitive magnetic probe, the μSR signal may be affected by the local fields created by the paramagnetic Nd^{3+} ions. A basic magnetic characterization of Nd_2O_3 was therefore undertaken using the magnetometer at the TAIL Facility of the University of Coimbra.

3.1 Temperature and field dependent measurements

A sample of Nd_2O_3 obtained commercially from Alfa Aesar, (REacton, with a degree of purity of 99.999%) was measured in the magnetometer. The mass of the sample was measured to be 7.84(2) mg. Both the temperature and the magnetic field dependence of the magnetic moment of the Nd_2O_3 sample were measured. For the temperature dependence the sample is subject to a range of temperature between 300 K and 1.8 K with a constant magnetic field of 100 Oe (fig 3.1). Both descending and ascending temperatures were measured in order to check for possible hysteretical behavior with temperature. No noticeable differences were observed. The

field dependence of the magnetic moment was investigated for five temperatures (1.8 K, 4 K, 10 K, 20 K, 50 K) varying the field between +9 T and -9 T. The results for $T=1.8$ K and $T=50$ K are shown in figure 3.2.

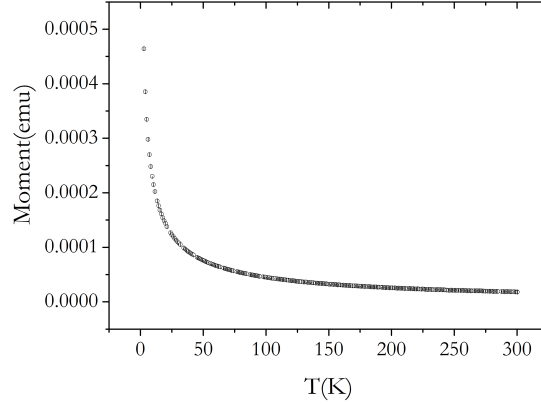


Figure 3.1: Magnetic moment of the Nd_2O_3 sample as a function of temperature, with an applied field of 100 Oe.

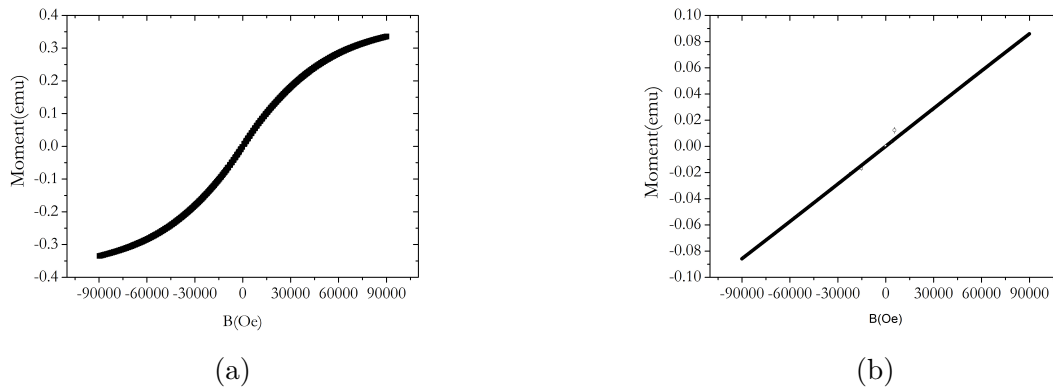


Figure 3.2: Magnetic moment of the Nd_2O_3 sample as a function of applied magnetic field, for $T=1.8$ K (a) and $T=50$ K (b)

In fig 3.2 we can appreciate the usual Brillouin-like behaviour of a paramagnet and thus verify no signs of the hysteresis behaviour typical of the onset of magnetic ordering. In principle the curves in Fig 3.2 should be fitted to a Brillouin curve but, as we will see immediately in the discussion of the temperature dependence in Fig 3.1, the behaviour at low-temperatures is significantly disturbed by the crystal field [PS32]. We will limit our discussion to the temperature dependence in fig 3.1. It is possible to see that the field dependent magnetic moment is practically linear at low fields. This is the region of interest for our study, because the magnetic field applied in the μSR is low (100 Oe).

3.2 Temperature dependence of susceptibility: Curie-Weiss model

The data in Fig 3.1 are conveniently analysed in terms of the magnetic susceptibility:

$$\chi = \frac{M}{H} \quad (3.1)$$

where M is the magnetization of the sample (magnetic moment per unit volume) and H is the applied magnetic field. This function can be easily formulated in terms of the mass of the sample taking into account that $M = \mu_s / V$ ($= \mu_s$ the total magnetic moment of the sample and V the sample volume) and $\rho = m / V$ (ρ the sample density and m the mass of the sample):

$$\frac{1}{\chi} = \frac{mH}{\rho\mu_s} \quad (3.2)$$

The density of Nd_2O_3 is 7.84 g.cm^{-3} [NdS].

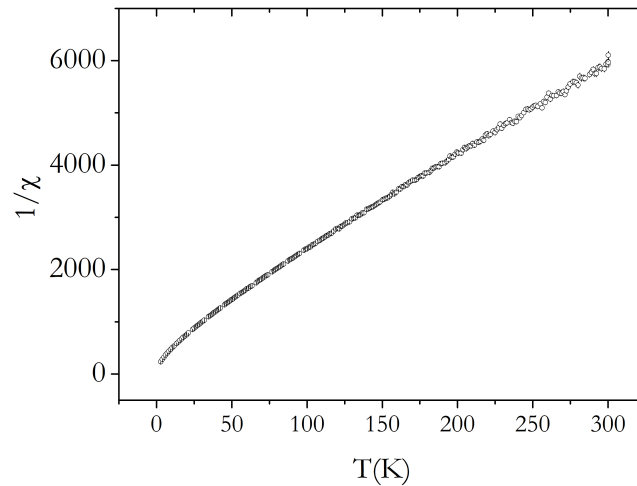


Figure 3.3: Inverse magnetic susceptibility of Nd_2O_3 as a function of temperature.

The uncertainty in χ^{-1} is essentially determined by that of the magnetic moment μ_s , particularly at high temperatures where μ becomes very small:

$$\sigma_{\frac{1}{\chi}} = \frac{\frac{1}{\chi}\sigma\mu}{\mu} \quad (3.3)$$

The graphic of the inverse susceptibility of Nd_2O_3 against temperature is shown in Fig 3.3 and a linear behaviour is clearly seen in the range of temperature between 200 K and 300 K. In this regime of temperature it is possible to apply the Curie-Weiss law [CSB11]:

$$\frac{1}{\chi} = \frac{T - T_0}{C} \quad (3.4)$$

In the Curie-Weiss model; $C=3k_B/n\mu^2\mu_0$, where k_B is the Boltzmann constant, $n=N/V$ is the concentration of magnetic ions ($n=2.5915 \cdot 10^{22} \text{ cm}^{-3}$) μ is the magnetic moment of each ion and μ_0 is the magnetic susceptibility in vacuum ($\mu_0 = 4\pi \cdot 10^{-7} \text{ A/m}$ in SI, 1 in electrostatic units) $\mu = \mu_B p_{eff}$, where the effective number p_{eff} of Bohr magnetons, μ_B is expected to be $p_{eff} = g\sqrt{J(J+1)}$ where J is total angular momentum of the ion and g is the Landé factor

$$g_J = \frac{3}{2} + \frac{S(S+1) - L(L+1)}{2J(J+1)} \quad (3.5)$$

The effective number of Bohr magnetons p_{eff} can be predicted using Hund rules, in order to establish for Nd^{3+} the values of the total angular momentum J , of the spin angular momentum S , and of the orbital angular momentum L . The Hund rules constitute a simple approach to find the configuration corresponding to the minimum energy of the system. The first rule is to maximize the value of S . The purpose is to reduce to Coulomb repulsion between electrons. To do this, we prevent the electrons with parallel spins being in the same m_l suborbitals. Nd^{3+} , has an outer shell 4f occupied with 3 electrons. The rule for the maximization of S implies that all spins are parallel, occupying different m_l . We therefore obtain $S=3/2$. The second Hund rule corresponds to maximizing the value of L . The objective is again to minimize the effect of Coulomb repulsion. This is achieved if the electrons successively occupy the m_l sub-orbitals with the highest value of m_l ($m_l=3, m_l=2, m_l=1$ as shown in fig 3.4). The total M_L is therefore $M_L=+3+2+1=+6$, corresponding to $L=6$. The third rule is to find the value of J . If the shell

is less than half-full, $J=L-S$ and if the shell is more than half full, $J=L+S$. The purpose of this rule is to minimize the spin-orbit energy. In our case we use the first condition. Because of that $J=9/2$ [Blu03].

	↑
$m_l=3$	●
$m_l=2$	●
$m_l=1$	●
$m_l=0$	
$m_l=-1$	
$m_l=-2$	
$m_l=-3$	

Figure 3.4: The ground state of Nd^{3+}

3.3 Determination of magnetic moment of Nd^{3+} from high temperature susceptibility

The fit of the inverse magnetic susceptibility of Nd_2O_3 at high temperatures (between $T = 200$ K and $T = 300$ K with Eq. 3.4 yields $C=17.34(14)$ and $T_0=-43(2)$ K (the negative value of T_0 is typical of an antiferromagnet). The effective number of Bohr magnetons p_{eff} can be immediately obtained.

$$P_{eff} = \frac{\sqrt{\frac{3 \cdot k_B}{C \cdot n}}}{\mu_B} \quad (3.6)$$

We obtain $p_{eff}=3.3(3)$ for Nd_2O_3 . This compares with the expected value (from Hund rules above) of $p_{eff}=3.62$. In the literature, experimental values between 3.3 and 3.7 are found[Blu03]. The fit clearly does not describe the data at low temperatures. In fact the Curie–Weiss model

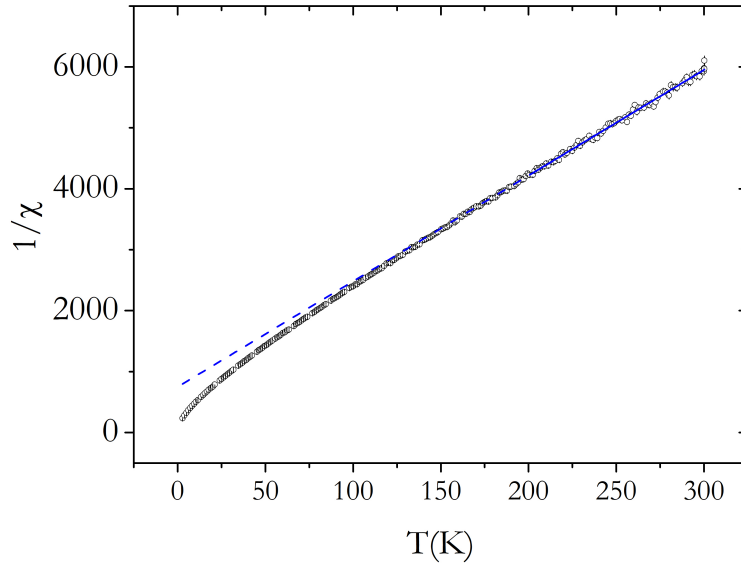


Figure 3.5: Magnetometry of Nd_2O_3 , plotting the inverse susceptibility against the temperature. The blue line is a fit of the Curie-Weiss law in the range of temperatures between 200 K and 300 K

does not have into consideration the spin-orbit interaction or the potential of the crystal field that has a great impact in the magnetic behaviour of Nd_2O_3 at low temperatures.

3.3.1 Temperature dependence of the susceptibility at low temperature

The ground state of Nd^{3+} is $J=9/2$. The excited multiplet with the lowest energy ($J=11/2$) is experimentally observed with an energy difference of 0.223 eV, corresponding to 1800 cm^{-1} and will be ignored in the following discussion. In the absence of any other interaction the ground state multiplet with $J=9/2$ corresponds to a 10-fold degeneracy. However, the electrostatic field felt by the Nd^{3+} in the crystalline environment (crystal-field) removes the degeneracy. The removal is not complete: Nd^{3+} having a half-integer spin, time-symmetry arguments imply that each energy level is at least doubly-degenerate (Kramers theorem)[PS32].

The structure of the ground-state multiplet of Nd^{3+} in the crystal electric field in Nd_2O_3 has been measured by several techniques:

1. By heat capacity measurements, where each level gives a Schottky anomaly (peak) in the heat capacity.
2. By optical absorption measurements, where 4 upper doublets have been measured at [JWJ63]:
 - (a) 21 cm^{-1} , 78 cm^{-1} , 244 cm^{-1} , and 491 cm^{-1} , [CDBS79] or at
 - (b) 23 cm^{-1} , 84 cm^{-1} , 253 cm^{-1} , 496 cm^{-1} [HMG67].

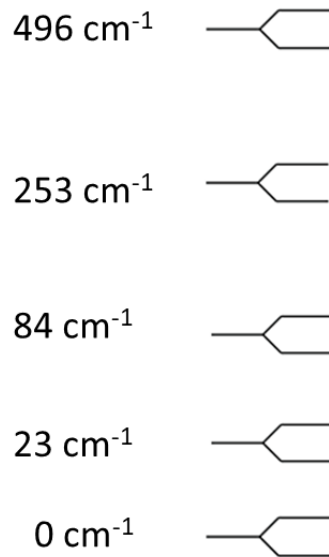


Figure 3.6: Energy levels of Nd^{3+} according to [HMG67]

These levels are sketched in Fig. 3.6. The transition from the lower doublet to the first excited doublet at 21 cm^{-1} (or 23 cm^{-1}) corresponds to a transition energy of 2.6 meV (or 2.85 meV), which can be thermally excited at a temperature of about 30 K (or 33 K).

In the presence of an external magnetic field, the levels are shifted. The usual linear Zeeman effect implies a change in energy of $m_J g \beta H$, where m_J is the quantum number for the projection of the total spin in the direction of the applied magnetic field H ; g is the Landé factor of the spin state; and β is the Bohr magneton. As seen in other Nd^{3+} systems, the linear Zeeman effect is not sufficient to describe the effect of the external field and a second-order effect is

necessary to describe the data (this is attributed to the impossibility to eliminate all the spacial degeneracy [PS32]).

We note that the energy eigenstates of the ground-state multiplet of Nd^{3+} in Nd_2O_3 will not in principle have a well-defined value of m_J . We have thus tried to model our susceptibility data assuming the following dependence with magnetic field of each of the 10 levels:

$$W_1 = a_1 H \beta + b_1 H^2, (m_1 \sim 3/2) \quad (3.7)$$

$$W_2 = -a_1 H \beta + b_1 H^2, (m_1 \sim -3/2) \quad (3.8)$$

$$W_3 = 7.2765 \times 10^{-16} + a_2 H \beta + b_2 H^2, (m_3 \sim 1/2) \quad (3.9)$$

$$W_4 = 7.2765 \times 10^{-16} - a_2 H \beta + b_2 H^2, (m_3 \sim -1/2) \quad (3.10)$$

$$W_5 = 2.6575 \times 10^{-16} + a_3 H \beta + b_3 H^2, (m_5 \sim 5/2) \quad (3.11)$$

$$W_6 = 2.6575 \times 10^{-16} - a_3 H \beta + b_3 H^2, (m_5 \sim -5/2) \quad (3.12)$$

$$W_7 = 8 \times 10^{-15} + a_4 H \beta + b_4 H^2, (m_7 \sim 9/2) \quad (3.13)$$

$$W_8 = 8 \times 10^{-15} - a_4 H \beta + b_4 H^2, (m_7 \sim -9/2) \quad (3.14)$$

$$W_9 = 1.5692 \times 10^{-15} + a_5 H \beta + b_5 H^2, (m_9 \sim 7/2) \quad (3.15)$$

$$W_{10} = 1.5692 \times 10^{-15} - a_5 H \beta + b_5 H^2, (m_9 \sim -7/2) \quad (3.16)$$

We indicate in parenthesis the estimated value of m_J for each level (from Ref. [CDBS79]). We also note that, for a question of simplicity and in order to be easier to compare our results with former results from literature, we have here used cgs units. The above-mentioned levels are thus in erg.

Knowing all the possible states of energy, it is possible to calculate the magnetic susceptibility using the following expression [PS32]:

$$X = -\frac{N}{H} \sum \frac{\partial W}{\partial H} e^{\frac{-W}{k_B T}} / \sum e^{\frac{-W}{k_B T}} \quad (3.17)$$

where H represents the magnetic field, T the temperature, k_B is the constant of Boltzmann, W are the energy levels and N is the total number of magnetic ions in the sample. We have thus fitted our magnetization curve with the above -expression for the susceptibility, using the energy-levels defined above. The parameters a_j and b_j , $j = 1, \dots, 5$ were the fitting parameters. The fit is shown in Fig. 3.7 and the resulting parameters are shown in table 3.1.

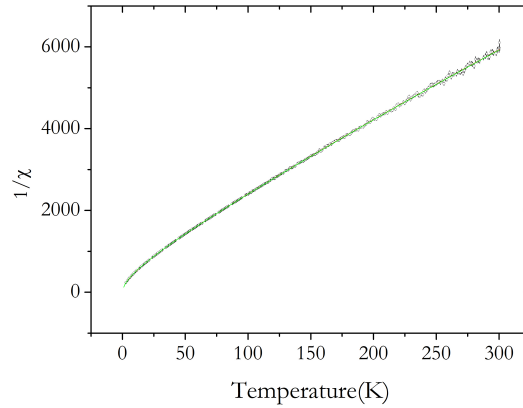


Figure 3.7: Fit to the magnetic susceptibility of Nd_2O_3 including the crystal-field effects, as described in the text.

Parameter	Value	Uncertainty
a1	-6.72E-21	3.41E-21
b1	-4.11E-27	1.18E-25
a2	1.28E-20	1.09E-20
b2	3.14E-27	2.44E-26
a3	-1.51E-20	1.27E-20
b3	-1.29E-26	6.02E-26
a4	2.11E-20	1.31E-20
b4	4.71E-26	7.13E-27
a5	2.86E-20	5.74E-21
b5	-3.46E-26	3.82E-26

Table 3.1: Linear and quadratic Zeeman effect parameters a_j and b_j estimated from the fit in Fig. 3.7

3.4 A metrology digression: rare-earth oxides as calibration standards in magnetometry

The origin of metrology, as we know it, begins in the turn from the eighteenth century to the nineteenth century, in France. The goal of its creation was to order and unify all regions of France using their own metric system. Another reason for its creation was the advent of mass production, as one factory would produce parts of a device and send it to another factory to be finished. It was then vital that there was an agreement in the measuring system used by both factories, in order to prevent mistakes [QK05].

The first standard metric system was created in France in 1799 with two units: the metre and the kilogram [BhS]. France was the first country to use this system, but other countries like Italy, Netherlands or Spain also used it. A problem of that system was that only France had the standard of measurements and could produce copies of it. To overcome this problem, the Bureau International des Poids et Mesures was founded in 1875. This institution had the mission of establishing the metric system throughout the world by constructing new prototypes and comparing them with the standard, as well as creating new methods to improve the certainty of the measurements [Hm]. Nowadays, the challenge of the Bureau International des Poids et Mesures and other international institutions of metrology is to find standards of measurements that only depend on fundamental physical constants [MMQ⁺11]. The metrology laboratories now play an essential role in science and in industry.

Two basic procedures can be followed in metrology: either the measurement is dependent on universal constants, for example the calibration of the voltage of one instrument by the Josephson Effect [TW89]; or one standard object is used as a prototype for the instruments. This object cannot exchange its chemical and physical structure during this time and should be easy to obtain in its pure state. The associated error in the equipment will be the correlation between the value that the referential measuring object gives and its expected value. The classical example of such a prototype is the Pt-Ir object used as the universal reference for the kilogram up to very recently [FFH05].

This last method is the one used for calibrating the magnetic moment obtained with a magnetometer. Precise value of the absolute magnetic moment of samples is relevant not only for condensed matter physics and materials science, but also for geomagnetism [Hos51].

Palladium is usually used for the calibration. The magnetometer at the TAIL Facility of University of Coimbra is provided with a palladium reference sample of the purest commercial available metal (Marz grade) with ferromagnetic impurities less than 30 ppm (as confirmed by independent analysis) The reference sheet provides the following table for the magnetic gram susceptibility at room temperature:

T (k)	Susceptibility($\chi_g * 10^{-6} \text{ cm}^{-3}/\text{g}$)
295	5.28
296	5.27
298	5.25
299	5.24

Table 3.2: Values of the susceptibility of Pd at different temperatures

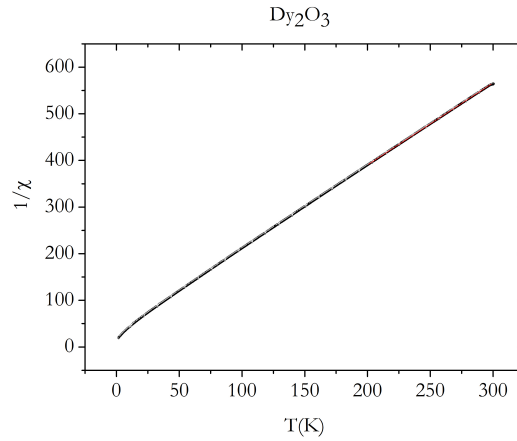
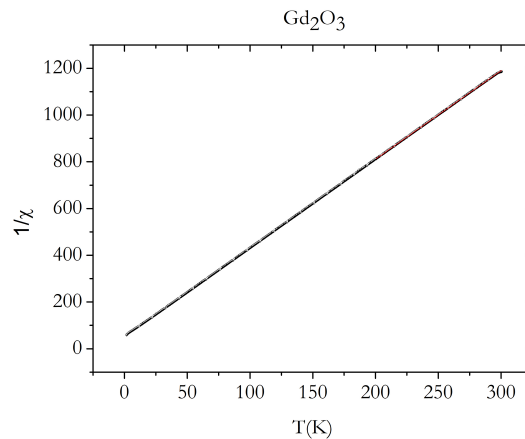
The magnetic gram susceptibility in table can be converted to the magnetic moment of the sample (in emu) by simply multiplying by the magnetic field (in G) and the mass of the sample (in g).

Paramagnetic rare-earth oxides have been systematically explored as calibration standards for magnetometry [PdL] This led us to explore the possibility of using these oxides as possible replacements and complements of the palladium standards provided by the manufacturer. The samples listed in table 3.3 were therefore investigated.

Sample	Reference	Purity%
Sm ₂ O ₃	Alfa AESAR	99.998
Gd ₂ O ₃	Alfa AESAR	99.999
Dy ₂ O ₃	Alfa AESAR	99.99
Ho ₂ O ₃	Alfa AESAR	99.995
Er ₂ O ₃	Alfa AESAR	99.99
Tm ₂ O ₃	Alfa AESAR	99.997
Yb ₂ O ₃	Alfa AESAR	99.998

Table 3.3: Rare-earth oxides investigated.

As an example of the results obtained, we show in figure 3.8 and 3.9 the temperature dependence of the inverse susceptibility of Gd₂O₃ and Dy₂O₃. As for Nd₂O₃, a magnetic field of 0.01T was applied to all samples and the temperature varied in the range 1.8 K to 300 K.

Figure 3.8: Inverse magnetic susceptibility of Gd₂O₃ as a function of temperature.Figure 3.9: Inverse magnetic susceptibility of Dy₂O₃ as a function of temperature.

Ion	S	L	J	g_J	p_{eff}
Sm^{3+}	5/2	5	5/2	4/3	0.85
Gd^{3+}	7/2	0	7/2	2	7.94
Dy^{3+}	5/2	5	15/2	4/3	0.85
Ho^{3+}	2	6	8	5/4	10.6
Er^{3+}	3/2	6	15/2	6/5	9.59
Tm^{3+}	1	5	6	1.17	7.57
Yb^{3+}	1/2	3	7/2	4/3	1.14

Table 3.4: Values of S,L,J, g_J , p_{eff} for each rare-earth ions

The resulting effective number p_{eff} of Bohr magnetons for each rare-earth ions was extracted in a similar way to that explained in section 3.2 and is shown in fig 3.10, as well as the corresponding expected values, obtained from the values in table 3.4.

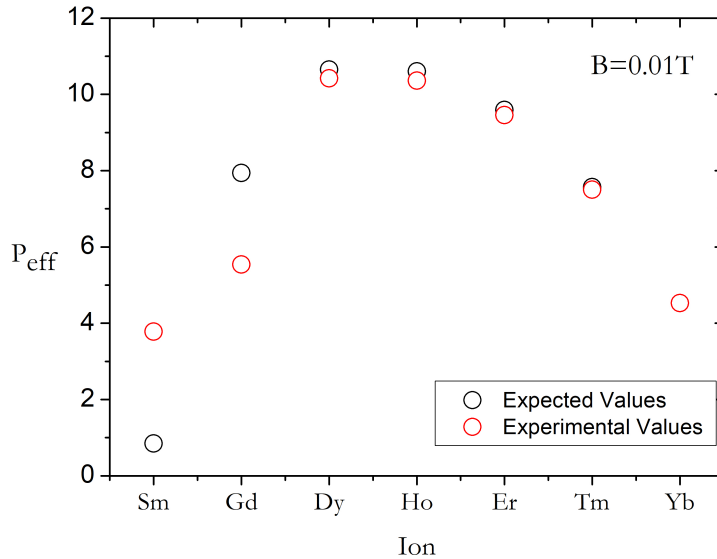


Figure 3.10: Comparison of the expected and experimental value of the effective number of Bohr magnetons for several rare-earth ions, p_{eff} . The error bars are smaller than the circles.

In fig 3.10 it is possible to see that the expected and experimental values agree quite well for most oxides. They are practically coincident in Yb^{3+} but some significant shifts are observed for Sm^{3+} and Gd^{3+} . The problematics of the correct determination of the susceptibility of Gd_2O_3 is thoroughly discussed in [FT11]. Antiferromagnetic interactions between some clustered Gd^{3+} ions have been mentioned in this and in previous literature [WHK⁺86]. Another problem that clearly emerges in ref. [FT11] is that most rare earth oxides are highly hygroscopic [GHW17],

which is bound to affect a precise and absolute measurement of the magnetic susceptibility.

Although these exploratory measurements by no means constitute a thorough and proper investigation of the use of rare-earth oxides as calibration standards, they provide some guideline that may be of use in future work in this research topic:

1. Yb_2O_3 seems to be a particularly good choice, although the precise reason is not apparent: is it less hygroscopic?
2. Dy_2O_3 , Ho_2O_3 , Er_2O_3 and Tm_2O_3 also provide particularly good results even in the absence of particular care with the sample treatment and conditioning before the magnetometer measurements;
3. Sm_2O_3 and Gd_2O_3 do not seem to be good choices for calibration standards; although Fukuma and Torii[FT11] have proved Gd_2O_3 to be adequate, it is apparent from their work that the use of these oxides for calibration requires an extreme care with the sample conditioning and experimental conditions; this does not make it the most obvious and easy choice.

Chapter 4

Muon Spin Spectroscopy Results

Muon spin spectroscopy experiments were performed at the EMU instrument of the ISIS Facility at the Rutherford-Appleton Laboratory (United Kingdom). In the experiments, a high-purity polycrystalline sample of Nd_2O_3 was used (obtained commercially from Alfa Aesar, REacton, 99.999%). Conventional muon spin rotation measurements were undertaken from $T = 8$ K up to $T = 640$ K with an applied transverse magnetic field $B = 0.01$ T. Calibration of the maximum asymmetry of the instrument was obtained using a silver sample.

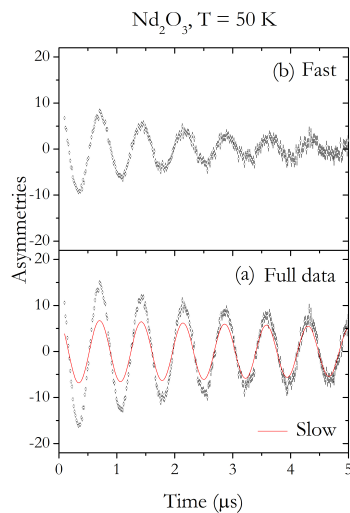


Figure 4.1: Time spectrum for a polycrystalline Nd_2O_3 sample at $T=50$ K and a transverse applied magnetic field $B=0.01$ T. (a) full data: the line represents the fitted slowly relaxing component, as detailed in the text. (b) fast relaxing component only, obtained from the fit as detailed in the text.

Figure 4.1 shows an asymmetry time spectrum obtained at $T = 50$ K and $B = 0.01$ T. The data can not be adequately fitted with a single relaxing component, and an additional component is needed to describe the data. These two components have significantly different relaxations λ_s and λ_f , and a slight difference between the corresponding precession frequencies f_s and f_f was also detected. The following fitting function was therefore used:

$$A(t) = A_s e^{(-\lambda_s t)} \cos(2\pi f_s t + \phi_s) + A_f e^{(-\lambda_f t)} \cos(2\pi f_f t + \phi_f) \quad (4.1)$$

where A_s and A_f are the asymmetries of the slowly relaxing and of the fast relaxing component, respectively; ϕ_s and ϕ_f are the corresponding initial phases. In order to illustrate the slow and fast components, we represent in Fig. 4.1 (a) the fitted slow component as a line and in Fig.4.1 (b) the complementary fast relaxing component. The relaxation λ_s is basically constant up to room temperature at $\lambda_s = 0.06 \mu\text{s}^{-1}$: this value is too small to allow a clear identification of the expected gaussian shape of the relaxation, so the lorentzian shape was used for convenience. The results are not affected by this ambiguity.

The WiMDA program was used for the data analysis and, after an intense preliminary analysis trying different approaches, we adopted the following final fitting procedure: firstly we determined the precession frequency and phase of the slow component from a fit to the room-temperature data ($T = 300$ K). These values were fixed in the low temperature range (from $T = 8$ K up to $T = 300$ K). Then a fit with two components was performed, fixing the phase of the fast component equal to that of the slow component. The precession frequency of the fast component was already found in the preliminary fitting to differ slightly from that of the slow component, so it was left as a free parameter.

The fast relaxing component is observed up to room temperature and our preliminary analysis indicates that the sum of the two components remains basically constant up to that temperature. We have thus fixed the sum constant in the final fits. Above room temperature, a single slowly relaxing component is sufficient to describe the data and it slowly grows with temperature up to achieving nearly 100% of the muon spin polarization at 640 K. The temperature dependence of the fraction of muons forming the slowly relaxing component and fast relaxing

component, F_s and F_f respectively, is represented in Fig 4.2. The fractions F_s and F_f were obtained from the ratios A_s/A_{max} and A_f/A_{max} , where A_{max} is the maximum instrumental asymmetry obtained with silver.

In Fig 4.3 we represent the temperature dependence of the relaxation λ_f of the fast component. An intense broadening of this line is observed above $T = 150$ K, concomitantly to the respective decrease of the fraction observed in Fig 4.2. At temperatures below 150 K, a slight reduction of the precession frequency f_f is observed for the fast component, with respect to the precession frequency f_s of the slow component, which in turn is basically identical to the precession frequency of the silver calibration sample at the same experimental conditions. In the final fits, f_s was therefore fixed. In Fig 4.4, we represent the temperature dependence of f_f .

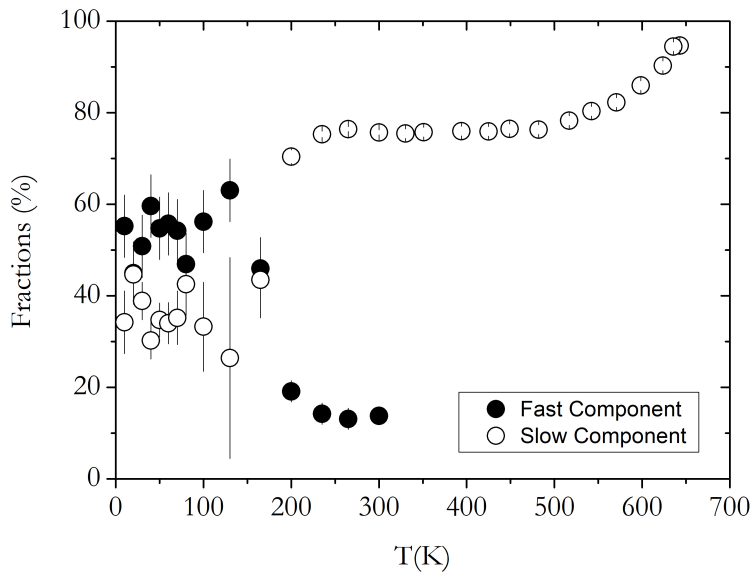


Figure 4.2: Temperature dependence of the slowly relaxing and of the fast relaxing components (white circles and black circles, respectively).

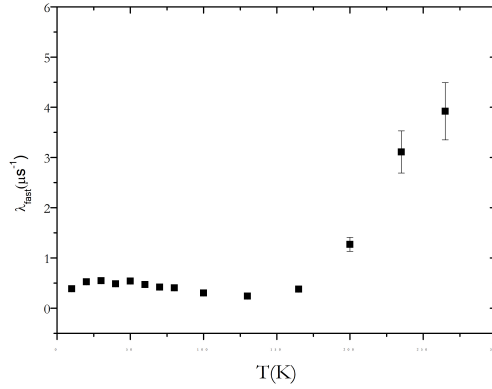


Figure 4.3: Temperature dependence of the relaxation of the fast component.

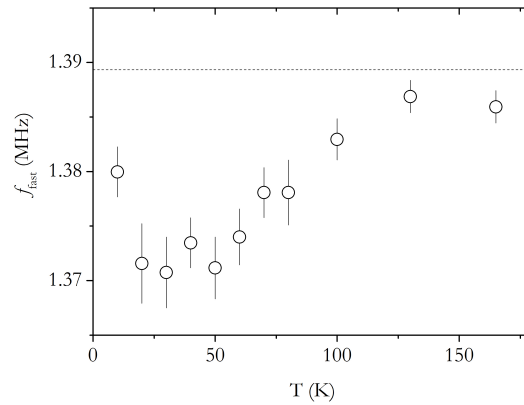


Figure 4.4: Temperature dependence of the precession frequency of the fast component, for an applied transverse magnetic field $B=0.01$ T. The dashed line is the value of precession frequency of a silver calibration sample in the same geometry.

Two temperature regions are immediately identified in fig 4.2:

1. below room temperature the fast and slow component coexist and their sum is approximately constant ($\sim 80\%$ of the total muon spin polarization); the remaining fraction of the muon spin polarization ($\sim 20\%$) is not observed (missing fraction);
2. above room temperature only the slow component is observed and it gradually grows with temperature until it corresponds to the full muon spin polarization at $T=700$ K.

4.1 Fast to slow conversion below $T= 300$ K

A clear conversion process is present below $T = 300$ K, the fast component converting to the slow one. This is visible not only in Fig 4.2 through the fraction interchange, but also in Fig 4.3 through the increase of relaxation of the fast component. The increase is typical of lifetime broadening, indicating a progressively reduced lifetime of the fast component.

The activation energy for the conversion can easily be estimated. We use a phenomenological Boltzmann-like model to describe the simultaneous change of F_s , F_f and λ_f with temperature:

$$F_f = B_D + \frac{F_0}{(1 + N_1 \exp(-E_{a1}/Tk_B))} \quad (4.2)$$

$$F_s = B_F + \frac{F_0 N_1 \exp(-E_{a1}/T)}{(1 + N_1 \exp(-E_{a1}/Tk_B))} \quad (4.3)$$

$$\lambda_f = B_R + \lambda_0 \exp(-E_{a1}/Tk_B) \quad (4.4)$$

where B_D , B_F and B_R are constants describing possible background components; N_1 is a density-of-states parameter; F_0 is the interconverting fraction; λ_0 is the pre-exponential factor for the activation of the relaxation. Most importantly, E_{a1} is the activation energy of the process, which is fixed equal in the simultaneous fit of equations 4.2, 4.3 and 4.4 to the corresponding data. An activation energy $E_{a1}=0.15(3)$ eV was obtained. The simultaneous fit is shown in figs 4.5 and 4.6

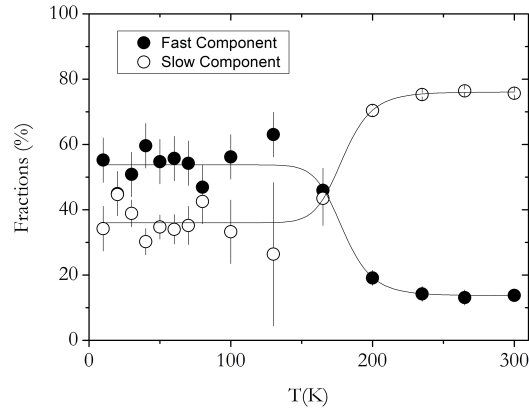


Figure 4.5: Temperature dependence of the slowly relaxing and of the fast relaxing components (white circles and black circles, respectively). The lines represent a common fit to the conversion from the fast to the slow component, as detailed in the text, with $E_a=0.15(3)$ eV

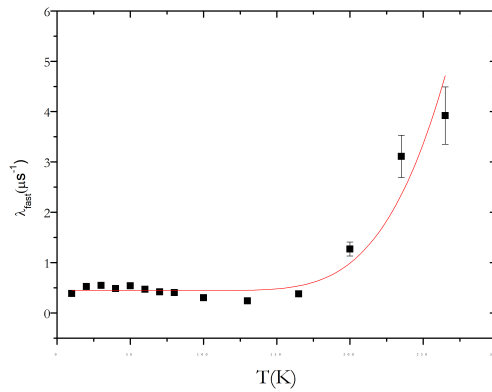


Figure 4.6: Temperature dependence of the relaxation of the fast component. The line is a fit of a conversion model from the fast component to the slow component, as explained in the text, with $E_a=0.15(3)$ eV.

4.1.1 Frequency shift of the fast component

A very prominent feature of the data below $T=150$ K is the presence of a frequency shift of the fast component. As shown in Fig 4.4, this is a negative frequency shift, the muon precession frequency being smaller than the pure Larmor frequency of the diamagnetic component (which is observed for the slow component and, of course, for the silver calibration).

The presence of a shift of the precession frequency is a clear signal of the presence of a paramagnetic interaction, where the muon spin is affected by the local field of a nearby electronic moment. In principle, the formation of a bound state of the positive muon and an electron

(muonium) does not create a negative shift: for the particular and exceptional cases where the muonium frequencies are close to muon diamagnetic Larmor frequency, they are either centered at the Larmor frequency (with an average zero shift) or slightly upward shifted (yielding a positive shift).

However, negative shift have been observed in the paramagnetic phase of ferromagnetic metals [WHK⁺86] and seen to follow the magnetization of the paramagnetic sample. A comparison of Fig.3.1 and Fig.4.4 immediately shows that the onset of the frequency shift is coincident with a significative increase of the magnetization below 150 K. The stabilization of the frequency shift and possible decrease below $T = 50\text{K}$ may in this interpretation be associated to the clustering of magnetic ions at lower temperatures, starting to develop local magnetic order. This has been proposal both in metallic Gd and in Gd_2O_3 .

4.2 Recovery of the missing fraction above 300 K

As mentioned already, 20 % of the spin polarization is not observed at low temperature (missing fraction). This missing fraction is basically constant up to room temperature. We recall that these data were acquired at the ISIS pulsed muon source. The muon beam pulse has a time width of 70 ns, implying that any signal faster then 14 MHz can not be detected. The missing fraction corresponds to one such extremely fast signal, that disappears either by fast precession or fast relaxation. In any case, the missing fraction corresponds to the presence of an extremely strong interaction affecting the muon spin, of unquestionable electronic origin.

As seen in Fig 4.2, above 300K the fraction of muons stopping at the slow component increases as the missing fraction decreases, again indicating a conversion process. An analysis with equation 4.3 to the increase of the slow component implies an activation energy $E_{a2} = 0.5(1)$ eV. The corresponding fit is shown in fig 4.7.

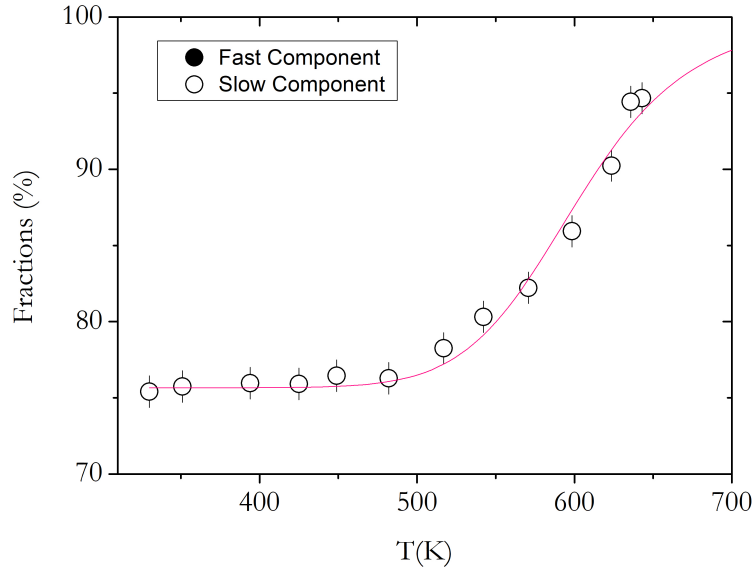


Figure 4.7: Temperature dependence of the slowly relaxing component. The full line is a fit to the conversion of the missing fraction to the slow component, as explained in the text, with $E_a = 0.5(1)$ eV.

4.2.1 Motional narrowing of the slow component

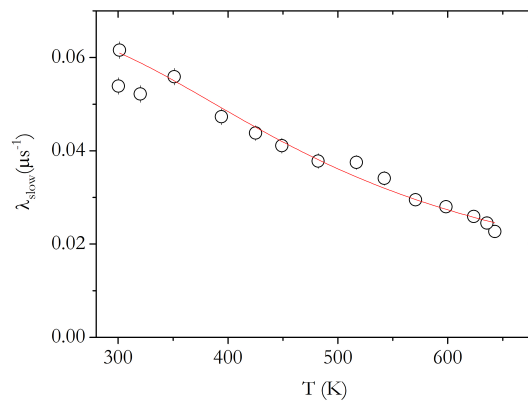


Figure 4.8: Temperature dependence of the relaxation of the slow component, above room temperature. The line is a fit of an activated process, as explained in the text below.

An additional phenomenon sets in above 300 K, as seen by the relaxation of the slow component (Fig 4.8). The relaxation visibly decreases with increasing temperature. We note that the extremely small value of the relaxation of the slow component points to a nuclear origin and corresponds to the known spread of the small magnetic field created by the nuclear magnetic

dipole moments (Nd has two magnetic isotopes: ^{143}Nd with $I=7/2$, $\mu=-1.065\mu_N$ and an abundance of 12 %, and ^{145}Nd with $I=7/2$, $\mu=-0.656\mu_N$ and an abundance of 8%). We therefore attribute this small relaxation $\lambda=0.06 \mu\text{s}^{-1}$ of the slow component at room temperature to the nuclear dipolar broadening. The decrease of this relaxation with increasing temperature is a well-known phenomenon corresponding to the narrowing of the dipolar field distribution which occurs when the muon starts moving (motional narrowing). Assuming once more that the motion of the muon is a thermally activated process, we analyse the data in fig 4.8 with a Boltzmann-like process:

$$\lambda_s = B_D + \frac{\lambda_o}{(1 + N_1 \exp(-E_{a1}/Tk_B))} \quad (4.5)$$

where B_D is a background relaxation (for example due to muons stopping in the sample holder), λ_o is the initial relaxation, N_1 is a density of states parameter and E_a is the activation energy. We obtain $E_a = 0.14(2) \text{ eV}$

4.3 Discussion

As we have seen above, the muon spin spectroscopy data in Nd_2O_3 reveal the presence of three components: a slowly relaxing component which becomes gradually dominant with temperature, a fast relaxing component characterized by a prominent negative frequency shift at low temperatures and an unobserved (missing) fraction that gives place to the slow component above room temperature. We begin the discussion of these components by the slowly relaxing component.

4.3.1 Slow component

The slowly relaxing component presents a small relaxation which, as pointed out above, is consistent with dipolar nuclear broadening only. It therefore does not present any evidence

of any interaction with an electronic moment, presenting a diamagnetic character. It thus likely correspond to either Mu^+ or Mu^- . These two species can not be distinguished with muon spin spectroscopy, but the formation of Mu^- implies the capture of two electrons after muon implantation, and this is a very unlikely process. We therefore assign the slowly relaxing component to the positively charged diamagnetic species Mu^+ .

The positively charged Mu^+ typically binds to the oxygen anion in oxides, forming a O-Mu bond [VVM⁺16] and it is therefore likely so also in Nd_2O_3 . The slow component therefore corresponds to this very stable oxygen-bound donor configuration in the Nd_2O_3 lattice (Fig 4.9).

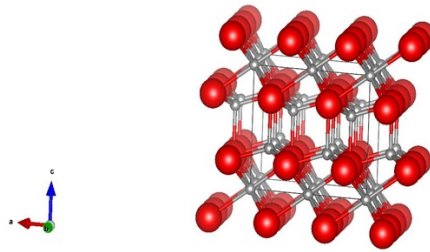


Figure 4.9: Crystal structure of Nd_2O_3 . The red circles are the oxygen ions and white circles are Nd ions.

4.3.2 Missing fraction

The missing fraction corresponds, as pointed out above, to a configuration subject to a strong paramagnetic interaction, leading to the fast disappearance of the muon spin polarization. We do not have any further data contributing to its characterization. In particular, the hyperfine interaction of this configuration could benefit from the recovery of the muon spin polarization in longitudinal fields: as the magnetic field is increased, the Zeeman interaction of the muon spin with the applied magnetic field becomes gradually dominant over the hyperfine interac-

tion, leading to the well-known repolarization curve [Pat88]. However, from the knowledge of similar oxide systems, it is likely that the missing fraction corresponds to the presence of a neutral paramagnetic state with a compact wavefunction and a correspondingly large hyperfine interaction. This neutral Mu^0 state is atomic-like and corresponds to the usual neutral version of the acceptor hydrogen configuration in oxides, which is typically found in interstitial sites of the lattice. The activation energy $E_a=0.5$ eV found in Fig. 4.7 for the conversion of the missing fraction to the slow component corresponds, in this interpretation, to the energy barrier for the site-change from the acceptor interstitial configuration to the donor oxygen-bound configuration.

4.3.3 Fast component

The fast component is the one which presents a more challenging interpretation. It corresponds to a muon state precessing at a diamagnetic-like frequency, which however is clearly affected by a near electronic moment providing the negative frequency-shift. It also corresponds to a fastly-relaxing state, which therefore is either short-lived or is subject to intense spin-fluctuation. Fast components as the one observed in Nd_2O_3 have been typically assigned to a short-lived diamagnetic species (Mu^+ or Mu^-) quickly converting to paramagnetic muonium (delayed muonium formation) [VVM⁺16]. However, Vilao et al. recently suggested that the fast component in oxides may actually correspond to a paramagnetic state with a very small hyperfine interaction (mostly dipolar-like) and fluctuating fast [VWA⁺17]. In the latter interpretation, this relaxing paramagnetic state corresponds to a transition state occurring before the muon reaches the final configurations (either donor-like or acceptor-like) and conditioning the final yield of the oxygen-bound to the atom-like configuration. A key aspect in the interpretation of Vilao et al. is that the observed frequency shift for the fast component in ZrO_2 is positive, as expected for a paramagnetic muonium species. The negative frequency shift observed for the fast component in Nd_2O_3 may possibly be made compatible with the transition state model attending to the fact that the magnetization is more intense at lower temperatures, implying that the electrons captured by the muon in the paramagnetic muon stage are spin-polarized according to the

magnetization. This electronic spin-polarization may be intense enough to justify a reversal of the frequency-shift. This negative-frequency shift would however not follow the magnetization curve [WHK⁺86] and the discrepancy is expected to be larger at low temperatures, where the muonium fraction is larger. This model would also explain why the frequency shift is observed in the fast component only (if it would be the result of the magnetization alone, both the slow and the fast components should be affected equally). These aspects however require more intense modelling, out of the scope of this project.

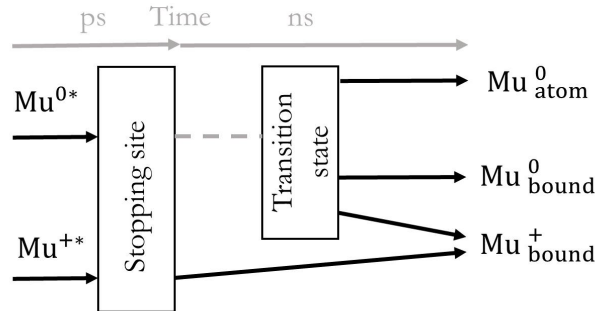


Figure 4.10: Final step in muon implantation: Neutral (Mu^0) and charged (Mu^+) muons come to rest at an interstitial site in the unrelaxed lattice (marked by *). Mu^+ forms directly the final bound configuration, but Mu^{0*} may go through an intermediate (transition) state before the final configuration is formed.

We reproduce in Fig 4.10 the transition-state model proposed by Vilao et al., which also provides adequate description of our data. In this model, the incoming muon may capture or not an electron in the slowing down process from the initial kinetic energy of 4 MeV. In the last stages of thermalization, the positive muons which have not captured an electron quickly find the only stable space for the positive configuration, at the oxygen-bound state.

The muons which capture an electron end up in the transition state and may proceed from there to one of the stable sites for the neutral configuration: either the acceptor-like Mu^0 atom state in an interstitial atom-like configuration or the donor-like Mu^0 bound in the oxygen-bound configuration. In this latter configuration the electron is typically loosely bound, and may be easily lost to the conduction band, so that the transition state may evolve directly to Mu^+_{bound} . The exit from the transition state to the corresponding stable neutral state is hindered by an energy barrier, which is dependent on the energy needed to change the lattice in order to accommodate the muon impurity. This lattice energy is typically much larger for the highly-distorted

oxygen-bound configuration than for the atomic-like interstitial configuration [DSMV⁺16]. The lifetime of the muon in the transition state proceeding to each one of the configurations will be therefore different, leading to different relaxations due to lifetime broadening. The higher the barrier, the higher the lifetime, the smaller the broadening. In this picture, the missing fraction corresponds to a very intense broadening from a small lifetime and a small barrier for the interstitial site, whereas the fast component corresponds to an observable (therefore) smaller relaxation due to a higher lifetime and a higher barrier to the distorted oxygen-bound site. Please note that while the reasoning above dictates that the fraction of muons arriving to the interstitial site from the transition state should be larger than those arriving at the oxygen-bound site, the slow component may actually be larger due to the fraction of muons arriving there directly from the muons which did not capture an electron in the slowing-down stage. Another important aspect is that the transition state is very quick, so that the final fractions are quickly frozen at their final values. In the model here pictured, the barrier from the transition state to the oxygen-bound configuration can be determined at higher temperatures when the thermal energy allows the muons to overcome the barrier thermally: the fractions of muons ending up in the fast component or in the slow component is therefore affected and the lifetime of the fast component becomes shorter (with a correspondingly increased relaxation). It is therefore not a conversion but a change in the formation probabilities of each component. The corresponding barrier thus corresponds to $E=0.15$ eV.

A scheme of the barrier model proposed for the observed components in Nd_2O_3 is presented in Fig 4.11

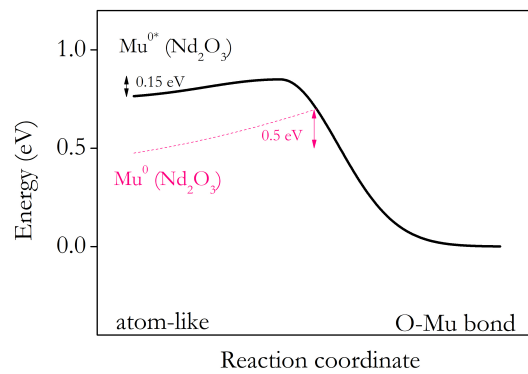


Figure 4.11: Schematic representation of the total energy for the conversion from atom-like interstitial to oxygen-bound muonium in Nd_2O_3 , including the value of the height of the energy barriers determined experimentally.

Chapter 5

Conclusion and Future Perspectives

5.1 Conclusions

The analysis of our muon spin spectroscopy data in Nd_2O_3 allows the identification of the basic muonium/hydrogen configurations in this paramagnetic rare-earth oxide. A slowly-relaxing diamagnetic component becomes gradually dominant as the temperature increases and is assigned to muons thermalizing in a donor-like oxygen-bound position. A significant fraction (c. 20%) of the muon spin polarization is missing at low temperatures and is recovered at high temperatures (above 300 K). This is assigned the muons thermalizing in the acceptor-like interstitial position. The thermally-activated conversion from the interstitial site to the oxygen bound site is observed above room temperature with an activation energy $E=0.5$ eV. A fast component is also detected and is assigned the muons in a paramagnetic transition state: to muon strongly interacts with an electron during the formation process and is affected by the electronic spin polarization through the magnetization of the sample, yielding a significant negative frequency-shift. The formation of the fast component is strongly affected by temperature, allowing to extract the height of the energy barrier separating it from the oxygen-bound configuration, that we estimate at $E=0.14$ eV from the thermal dependence. Overall, the basic μSR data is quite similar to those observed in other oxide systems, like ZrO_2 [VVM⁺16] or the diamagnetic rare-earth oxide Y_2O_3 [SMV⁺12]. The only effect of the sample paramagnetism is

the observed negative frequency shift. We thus conclude that μ SR can successfully probe the hydrogen configurations in Nd_2O_3 .

5.2 Future Perspectives

The current data in Nd_2O_3 constitute an important step in the investigation of the hydrogen configurations in rare-earth paramagnetic oxides by the muon spectroscopy techniques. Although our interpretation is strongly anchored in the existing literature of μ SR in oxides, many aspects could benefit from a deeper experimental approach.

5.2.1 Repolarization at low temperatures

As mentioned previously, the hyperfine interaction associated to the missing fraction can be estimated in longitudinal field experiments by varying the longitudinal field from zero to high values. As the Zeeman interaction becomes dominant over the hyperfine interaction, the observed muon spin polarization is increasingly larger. The observed muon spin polarization as a function of applied longitudinal field follows then a known repolarization behaviour, which is a direct measure of the hyperfine interaction.

5.2.2 Frequency shift

The frequency shift in Nd_2O_3 needs a more refined model that takes into account the negative contribution from the sample magnetization and the positive contribution due to the likely formation of a paramagnetic transition state. The effect of the sample magnetization implies a linear variation with applied magnetic field, so additional experiments in low transversal fields may be helpful. The negative frequency shift is also proportional, in principle to the magnetic moment of the rare-earth ion, so it would also be useful to check it by low transversal field in other rare-earth oxides (Cf. Fig. 4.4). In principle, the frequency shift should follow the

susceptibility of the material and the oxides that present a high value of susceptibility are expected to have a larger frequency shift.

5.2.3 Extension to other rare-earth oxides

A natural consequence of the study now presented is the possibility of exploring the hydrogen configurations in the other paramagnetic rare-earth oxides. Preliminary data have been obtained at the EMU instrument of the ISIS facility in samarium oxide Sm_2O_3 . Only a reasonable statistics spectrum was obtained at $T=8\text{K}$, which is shown in Fig 5.1.

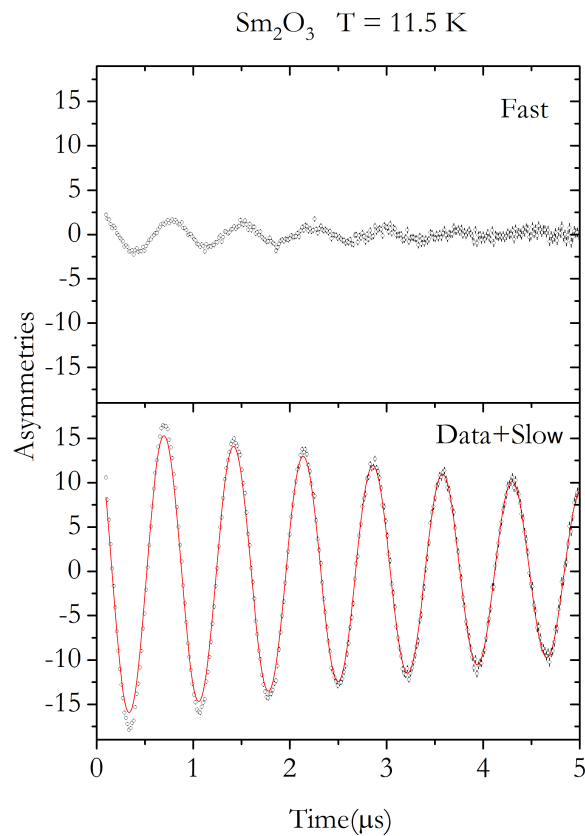


Figure 5.1: Time spectrum for a polycrystalline Sm_2O_3 sample at $T=50\text{ K}$ and a transversal applied magnetic field $B=0.01\text{T}$. The upper graphic is the representation of the fast component and in the bottom plot we present the full data; the red line is the fit to the slow component only.

The time spectrum shown in Fig 5.1 clearly presents a slow and a fast component as in Nd_2O_3 . It is therefore very likely that a similar behaviour is found when completing a temperature

dependence study as that obtained for Nd_2O_3 .

Bibliography

- [Beaa] ISIS pulsed muon source. <http://nmi3.eu/muon-research/where/isis.html>. Accessed: 2017-06-24.
- [Beab] More about muons:The characteristics of muons. <http://nmi3.eu/muon-research/characteristics-of-muons.html>. Accessed: 2017-06-24.
- [BhS] Brief history of the SI bureau international des poids et mesures. <http://www.bipm.org/en/measurement-units/history-si/>. Accessed: 2017-07-11.
- [Blu99] SJ Blundell. Spin-polarized muons in condensed matter physics. *Contemporary Physics*, 40(3):175–192, 1999.
- [Blu03] Stephen Blundell. Magnetism in condensed matter, 2003.
- [BPJ03] Wesley Burgei, Michael J Pechan, and Herbert Jaeger. A simple vibrating sample magnetometer for use in a materials physics course. *American Journal of Physics*, 71(8):825–828, 2003.
- [BRI14] TO BRIGHT. Efficient blue light-emitting diodes leading to bright and energy-saving white light sources. *Sci. Backgr. Noble Prize Phys*, pages 1–9, 2014.
- [Can] CAN Bus Module Tutorial for Arduino, Raspberry Pi and Intel Galileo. <https://www.cooking-hacks.com/documentation/tutorials/can-bus-module-shield-tutorial-for-arduino-raspberry-pi-intel-galileo/>. Accessed: 2017-06-24.

- [CDBS79] P Caro, J Derouet, L Beaury, and E Soulie. Interpretation of the optical absorption spectrum and of the paramagnetic susceptibility of neodymium a-type sesquioxide. *The Journal of Chemical Physics*, 70(5):2542–2549, 1979.
- [CDC⁺01] SFJ Cox, EA Davis, SP Cottrell, PJC King, JS Lord, JM Gil, HV Alberto, RC Vilão, J Piroto Duarte, N Ayres de Campos, et al. Experimental confirmation of the predicted shallow donor hydrogen state in zinc oxide. *Physical Review Letters*, 86(12):2601, 2001.
- [CSB11] D-X Chen, Vassil Skumryev, and B Bozzo. Calibration of ac and dc magnetometers with a dy_2o_3 standard. *Review of Scientific Instruments*, 82(4):045112, 2011.
- [DNZ⁺04] L Dobaczewski, K Bonde Nielsen, N Zangenberg, B Bech Nielsen, AR Peaker, and VP Markevich. Donor level of bond-center hydrogen in germanium. *Physical Review B*, 69(24):245207, 2004.
- [DSMV⁺16] E Lora Da Silva, AG Marinopoulos, RBL Vieira, RC Vilão, HV Alberto, JM Gil, RL Lichti, PW Mengyan, and BB Baker. Electronic structure of interstitial hydrogen in lutetium oxide from dft+ u calculations and comparison study with μ sr spectroscopy. *Physical Review B*, 94(1):014104, 2016.
- [Dyn11] Physical property measurement system dynacooltm users manual. Technical report, Quantum Design, 2011.
- [FFH05] Thomas Fehling, Thomas Fröhlich, and Detlef Heydenbluth. The new sartorius 1 kg prototype balance for high precision mass determination. In *Proc. 19th Int. Conf. on Force, Mass & Torque IMEKO TC3, Cairo (Egypt)*, pages 51–1, 2005.
- [FS07] Marco Fanciulli and Giovanna Scarel. *Rare Earth Oxide Thin Films*. Springer, 2007.
- [FT11] Koji Fukuma and Masayuki Torii. Absolute calibration of low-and high-field magnetic susceptibilities using rare earth oxides. *Geochemistry, Geophysics, Geosystems*, 12(7), 2011.

- [GAV⁺01] JM Gil, HV Alberto, RC Vilão, J Piroto Duarte, N Ayres de Campos, A Weidinger, J Krauser, EA Davis, SP Cottrell, and SFJ Cox. Shallow donor muonium states in ii-vi semiconductor compounds. *Physical Review B*, 64(7):075205, 2001.
- [GCK⁺14] SR Giblin, SP Cottrell, PJC King, S Tomlinson, SJS Jago, LJ Randall, MJ Roberts, J Norris, S Howarth, QB Mutamba, et al. Optimising a muon spectrometer for measurements at the isis pulsed muon source. *Nuclear Instruments and Methods in Physics Research Section A: Accelerators, Spectrometers, Detectors and Associated Equipment*, 751:70–78, 2014.
- [GHW17] Kian Heng Goh, ASMA Haseeb, and Yew Hoong Wong. Lanthanide rare earth oxide thin film as an alternative gate oxide. *Materials Science in Semiconductor Processing*, 68:302–315, 2017.
- [GLW57] Richard L Garwin, Leon M Lederman, and Marcel Weinrich. Observations of the failure of conservation of parity and charge conjugation in meson decays: the magnetic moment of the free muon. *Physical Review*, 105(4):1415, 1957.
- [HHL⁺02] Detlev M Hofmann, Albrecht Hofstaetter, Frank Leiter, Huijuan Zhou, Frank Henecker, Bruno K Meyer, Sergei B Orlinskii, Jan Schmidt, and Pavel G Baranov. Hydrogen: a relevant shallow donor in zinc oxide. *Physical Review Letters*, 88(4):045504, 2002.
- [HJF80] EE Haller, B Joos, and LM Falicov. Acceptor complexes in germanium: Systems with tunneling hydrogen. *Physical Review B*, 21(10):4729, 1980.
- [HL98] G Heine and W Lang. Magnetoresistance of the new ceramic cernox thermometer from 4.2 k to 300k in magnetic fields up to 13t. *Cryogenics*, 38(4):377–379, 1998.
- [Hm] History of measurement. <https://web.archive.org/web/20110425025041/http://www.frenchmetrology.com/en/history/history-measurement.asp> . Accessed: 2017-07-11.
- [HMG67] JR Henderson, M Muramoto, and John B Gruber. Spectrum of nd^{3+} in lanthanide oxide crystals. *The Journal of Chemical Physics*, 46(7):2515–2520, 1967.

- [Hos51] J Hospers. Remanent magnetism of rocks and the history of the geomagnetic field. *Nature*, 168:1111–1112, 1951.
- [INMS15] Rutherford Appleton Laboratory ISIS Neutron Muon Source. The emu user guide. Technical report, Science Technology Facilities Council, 2015.
- [JWJ63] Bruce H Justice and Edgar F Westrum Jr. Thermophysical properties of the lanthanide oxides. i. heat capacities, thermodynamic properties, and some energy levels of lanthanum (iii) and neodymium (iii) oxides from 5 to 350 k. *The Journal of Physical Chemistry*, 67(2):339–345, 1963.
- [KPPN05] Anne Kosola, Jani Päiväsaari, Matti Putkonen, and Lauri Niinistö. Neodymium oxide and neodymium aluminate thin films by atomic layer deposition. *Thin Solid Films*, 479(1):152–159, 2005.
- [LCC08] RL Lichti, KH Chow, and SFJ Cox. Hydrogen defect-level pinning in semiconductors: The muonium equivalent. *Physical review letters*, 101(13):136403, 2008.
- [LCG⁺06] RL Lichti, KH Chow, JM Gil, DL Stripe, RC Vilão, and SFJ Cox. Location of the h [+/-] level: Experimental limits for muonium. *Physica B: Condensed Matter*, 376:587–590, 2006.
- [LCK99] Stephen L Lee, R Cywinski, and SH Kilcoyne. *Muon science: Muons in physics, chemistry and materials*, volume 51. CRC Press, 1999.
- [LFR⁺05] R Lupták, K Fröhlich, A Rosová, K Hušková, M Ľapajna, D Machajdik, Matej Jergel, JP Espinós, and C Mansilla. Growth of gadolinium oxide films for advanced mos structure. *Microelectronic engineering*, 80:154–157, 2005.
- [LY56] Tsung-Dao Lee and Chen-Ning Yang. Question of parity conservation in weak interactions. *Physical Review*, 104(1):254, 1956.
- [MMQ⁺11] Ian M Mills, Peter J Mohr, Terry J Quinn, Barry N Taylor, and Edwin R Williams. Adapting the international system of units to the twenty-first century. *Phil. Trans. R. Soc. A*, 369(1953):3907–3924, 2011.

- [Mos] What is MOSFET with Working? MOSFET as a Switch.
<https://www.elprocus.com/mosfet-as-a-switch-circuit-diagram-free-circuits/>.
Accessed: 2017-07-15.
- [MSK⁺12] Yasuhiro Miyake, Koichiro Shimomura, Naritoshi Kawamura, Patrick Strasser, Akihiko Koda, Shunsuke Makimura, Hiroshi Fujimori, Yutaka Ikedo, Kazutaka Nakahara, Soshi Takeshita, et al. J-parc muon facility, muse. *Physics Procedia*, 30:46–49, 2012.
- [NdS] Nd₂O₃. <http://www.sigmaaldrich.com/catalog/product/aldrich/203858?lang=ptregion=PT/>
Accessed: 2017-07-14.
- [Nic99] Norbert H Nickel. Introduction to hydrogen in semiconductors ii. *Semiconductors and Semimetals*, 61:1–11, 1999.
- [NPP⁺05] Jaakko Niinistö, Nikolina Petrova, Matti Putkonen, Lauri Niinistö, Kai Arstila, and Timo Sajavaara. Gadolinium oxide thin films by atomic layer deposition. *Journal of crystal growth*, 285(1):191–200, 2005.
- [NVdW95] Jörg Neugebauer and Chris G Van de Walle. Hydrogen in gan: novel aspects of a common impurity. *Physical review letters*, 75(24):4452, 1995.
- [Pat88] Bruce D Patterson. Muonium states in semiconductors. *Reviews of modern physics*, 60(1):69, 1988.
- [PdL] Palladium reference sample. Technical report, Quantum Design.
- [PPN05] Jani Päiväsaari, Matti Putkonen, and Lauri Niinistö. A comparative study on lanthanide oxide thin films grown by atomic layer deposition. *Thin Solid Films*, 472(1):275–281, 2005.
- [PPSN04] Jani Päiväsaari, Matti Putkonen, Timo Sajavaara, and Lauri Niinistö. Atomic layer deposition of rare earth oxides: erbium oxide thin films from β -diketonate and ozone precursors. *Journal of alloys and compounds*, 374(1):124–128, 2004.

- [PS32] William G Penney and Robert Schlapp. The influence of crystalline fields on the susceptibilities of salts of paramagnetic ions. i. the rare earths, especially pr and nd. *Physical Review*, 41(2):194, 1932.
- [PSI] LMU: Laboratory for Muon Spin Spectroscopy. <https://www.psi.ch/lmu/>. Accessed: PSI017.
- [QK05] Terry Quinn and Jean Kovalevsky. The development of modern metrology and its role today. *Philosophical Transactions of the Royal Society of London A: Mathematical, Physical and Engineering Sciences*, 363(1834):2307–2327, 2005.
- [Rad09] Ray Radebaugh. Cryocoolers: the state of the art and recent developments. *Journal of Physics: Condensed Matter*, 21(16):164219, 2009.
- [RN09] Mikko Ritala and Jaakko Niinistö. Atomic layer deposition. *Chemical Vapor Deposition: Precursors, Processes and Application*, pages 158–206, 2009.
- [Rob04] J Robertson. High dielectric constant oxides. *The European Physical Journal-Applied Physics*, 28(3):265–291, 2004.
- [Sah10] Samar K Saha. Modeling process variability in scaled cmos technology. *IEEE Design & Test of Computers*, 27(2), 2010.
- [SBK00] Jeff E Sonier, Jess H Brewer, and Robert F Kiefl. μ sr studies of the vortex state in type-ii superconductors. *Reviews of Modern Physics*, 72(3):769, 2000.
- [SM08] J. Singh and U.K. Mishra. *Semiconductor Device Physics and Design*. Springer, 2008.
- [SMV⁺12] EL Silva, AG Marinopoulos, RC Vilão, RBL Vieira, HV Alberto, J Piroto Duarte, and JM Gil. Hydrogen impurity in yttria: Ab initio and μ sr perspectives. *Physical Review B*, 85(16):165211, 2012.
- [Tp] Temperature products. <http://www.lakeshore.com/products/Cryogenic-Temperature-Sensors/Cernox/Models/Pages/Specifications.aspx>. Accessed: 2017-06-24.

- [TRI] Centre for Molecular Materials Science. <http://www.triumf.ca/research/research-facilities/centre-for-molecular-materials-science>. Accessed: 2017-06-28.
- [TW89] BN Taylor and TJ Witt. New international electrical reference standards based on the josephson and quantum hall effects. *Metrologia*, 26(1):47, 1989.
- [VdW00] Chris G Van de Walle. Hydrogen as a cause of doping in zinc oxide. *Physical review letters*, 85(5):1012, 2000.
- [VdW06] Chris G Van de Walle. Universal alignment of hydrogen levels in semiconductors and insulators. *Physica B: Condensed Matter*, 376:1–6, 2006.
- [VdWN03] Chris G Van de Walle and Jörg Neugebauer. Universal alignment of hydrogen levels in semiconductors, insulators and solutions. *Nature*, 423(6940):626, 2003.
- [VGW⁺07] RC Vilão, JM Gil, A Weidinger, HV Alberto, J Piroto Duarte, N Ayres de Campos, RL Lichti, KH Chow, and SFJ Cox. Information on hydrogen states in ii–vi semiconductor compounds from a study of their muonium analogues. *Nuclear Instruments and Methods in Physics Research Section A: Accelerators, Spectrometers, Detectors and Associated Equipment*, 580(1):438–441, 2007.
- [VGW⁺08] RC Vilao, JM Gil, A Weidinger, HV Alberto, J Piroto Duarte, N Ayres de Campos, RL Lichti, KH Chow, SP Cottrell, and SFJ Cox. Acceptor level of interstitial muonium in znse and zns. *Physical Review B*, 77(23):235212, 2008.
- [VVA⁺14] RBL Vieira, RC Vilão, HV Alberto, JM Gil, A Weidinger, BB Baker, PW Mengyan, and RL Lichti. High-field study of muonium states in hfo₂ and zro₂. In *Journal of Physics: Conference Series*, volume 551, page 012048. IOP Publishing, 2014.
- [VVA⁺15] RC Vilão, RBL Vieira, HV Alberto, JM Gil, A Weidinger, RL Lichti, BB Baker, PW Mengyan, and JS Lord. Muonium donor in rutile tio₂ and comparison with hydrogen. *Physical Review B*, 92(8):081202, 2015.

- [VVM⁺16] RBL Vieira, RC Vilão, AG Marinopoulos, PM Gordo, JA Paixão, HV Alberto, JM Gil, A Weidinger, RL Lichti, B Baker, et al. Isolated hydrogen configurations in zirconia as seen by muon spin spectroscopy and ab initio calculations. *Physical Review B*, 94(11):115207, 2016.
- [VWA⁺17] R. C. Vilão, A. Weidinger, H. V. Alberto, R. B. L. Vieira, and J. M. Gil. On the interpretation of the fast relaxing signal in sr experiments. *The 14th International Conference on Muon Spin Rotation, Relaxation and Resonance, Book of Abstracts*, O34:187, 2017.
- [WHK⁺86] E Wäckelgård, O Hartmann, E Karlsson, R Wäppling, L Asch, GM Kalvius, J Chappert, and A Yaouanc. Knight shifts and relaxation in gadolinium above the curie temperature. *Hyperfine Interactions*, 31(1):325–330, 1986.
- [YDdR11] A. Yaouang and P. Dalmas de Retier. *Muon spin rotation, relaxation and resonance*, volume 1. Oxford University Press, 2011.